Dynamic Heights and Zonal Geostrophic Transports in the Central Tropical Pacific during 1979–84

WILLIAM S. KESSLER

School of Oceanography, University of Washington, Seattle, WA 98195

BRUCE A. TAFT

Pacific Marine Environmental Laboratory/NOAA, Seattle, WA 98115

ABSTRACT

Dynamic height is calculated from XBT and surface salinity data in the central Pacific using a mean temperature–salinity (T–S) relation in the usual way below the thermocline but assuming isohaline water in the upper layer where the temperatures are isothermal. This scheme produces a better estimate of dynamic height than the use of a mean T–S relationship alone and produces significant improvements near the equator where small pressure gradients imply large geostrophic currents.

During the El Niño of 1982–83, water of very low surface salinity was observed spanning the equator; this event is attributed both to extreme local rainfall and anomalous advection from the western Pacific. Geostrophic transports of the major surface currents are estimated for the period January 1979 through December 1984. The North and South Equatorial countercurrents are found to have the largest annual fluctuations, and the vertical displacements of the thermocline associated with these fluctuations are qualitatively consistent with local Ekman pumping.

A striking anomaly of the 1982–83 El Niño was a strong peak in North Equatorial Countercurrent transport in late 1982; at this time surface flow was eastward from 10°N to 5°S with volume transport on the order of 60–70 × 10^6 m^3 s^{-1}. In mid-1983 NECC transport fell to less than 2 × 10^6 m^3 s^{-1}. During the first four months of 1983 strong westerlies extended from the equator to about 10°S over a broad region in the central Pacific. The wind curl pattern associated with this anomaly led to shoaling of the thermocline by 60 m from 5° to 15°S.

1. Introduction

Expendable bathythermographs (XBTs) have been deployed since 1979 from merchant ships operating out of Noumea, New Caledonia, under a joint United States–France ship of opportunity (SOP) program. The ships traverse nearly meridional routes in the central and western Pacific and an oblique route between Panama and Tahiti. In addition, surface temperature and salinity have been measured on these routes since 1975. This program has produced the only long time series of large-scale subsurface conditions in the tropical Pacific. Previous programs to measure the subsurface thermal field did not exceed 18 months, e.g., Trade Wind Zone Oceanography Study (TWZOS), February 1964 to June 1965 (Meyers, 1975; Seckel, 1975), and the Hawaii–Tahiti Shuttle Experiment, February 1979 to June 1980 (Wyrtki et al., 1981; Wyrtki and Kilonsky, 1984).

Although the SOP program produces spatially and temporally irregular data, it is the only presently available method for continuously monitoring large-scale subsurface thermal variability in the Pacific. Section 2 of this paper describes the data and discusses the problems and errors arising from the irregular SOP data collection.

The TWZOS and Hawaii–Tahiti Shuttle Experiments were based on CTD observations, so the calculation of density was straightforward. The present work shows that tropical central Pacific upper ocean density and geostrophic flow can be reliably estimated from temperature profiles and surface salinity data alone. In section 3, a scheme is developed for the estimation of density above the thermocline using these data. Essentially, the scheme assumes that the surface-layer salinity profile down to the mid-thermocline has the same functional form as does the temperature profile. Dynamic heights calculated by this method are significantly more accurate than those found using a mean T–S relation in the upper water column.

Description of the strong annual cycles of zonal geostrophic transport is central to an understanding of the fluctuations of heat content in the tropical Pacific. In section 4, it is shown that the North and South Equatorial countercurrents have the largest and most regular annual cycles, and that these are closely related to annual thermocline depth variations. In contradiction to earlier work based on shorter-term studies (Meyers,

1975), the North Equatorial Current is found to have only small annual volume transport variation. Furthermore, there is significant annual meandering of the zonal currents, which must be taken into account in order to accurately estimate volume transports.

The data record encompasses the strong El Niño of 1982–83; section 5 discusses the surface salinity, thermocline depth and volume transport fluctuations that were associated with this event. It is found that major thermocline depth anomalies associated with the El Niño event persisted at least through the middle of 1984. Satellite-derived wind data (Sadler and Kilonsky, 1985) are used in section 6 to compute Ekman pumping due to the curl of the wind stress; the inferred vertical motion is compared to vertical displacements of the thermocline in order to explore the role of this local dynamical mechanism. Annual fluctuation of North Equatorial Countercurrent transport is found to be related to thermocline depth variations induced by Ekman pumping, as noted by previous studies (Meyers, 1979). In addition, this mechanism is shown to be similarly responsible for much of the annual variability in the South Equatorial Countercurrent. During the 1982–83 El Niño event, strong wind anomalies (Sadler and Kilonsky, 1983) produced anomalous wind stress curl patterns. Strong Ekman pumping in the Southern Hemisphere associated with these anomalies is shown to be closely related to extra-equatorial thermocline shoaling during this period.
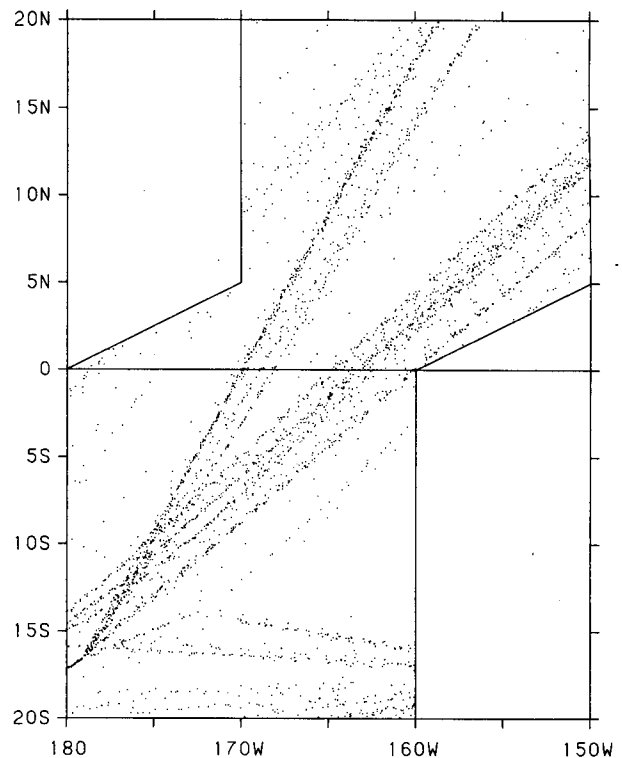

FIG. 1. Geographical scatter of all casts from the ship of opportunity program on the CP track for the period 1979 through June 1985 showing the outline of the section.

2. Data

Two sets of XBT data were used in the analysis. The primary set has been collected from ships of opportunity operating out of Noumea, New Caledonia (Meyers and Donguy, 1980); this program has been operating since 1979 and, in addition, has provided the surface temperature and salinity measurements used here. Only data from the central Pacific (CP) tracks (Noumea to Hawaii and the U.S. west coast), which run from about 20°S, 180° to 20°N, 150°W (Fig. 1), are discussed. A total of 3494 XBT profiles were made on this track between September 1979 and June 1985, or about 1.1 profiles per degree latitude per month. The sampling rate on the CP track has generally increased since the beginning of the program; 94 probes were deployed in 1979, 457 in 1980, 674 in 1981, 715 in 1982, 796 in 1983, 539 (received to date) in 1984, and 220 in the first six months of 1985. Figure 1 shows the geographical scatter of the casts.

The T4 XBT samples nominally to 450 m; in fact, 96% of the casts on the CP track reached 200 m, 92% reached 300 m, and 75% reached 400 m. Data are obtained approximately every 3.7 m in the vertical. Bucket sea-surface temperatures averaged 0.1°C higher than the 3.7 m XBT temperature at the same location. Kessler et al. (1985) evaluated the sensitivity of the estimation of dynamic height from this dataset to varied

XBT sampling rates. They also showed that during the Hawaii–Tahiti Shuttle (Wyrtki et al., 1981) 81% of the 0/1000 db dynamic height variance was due to variability in the upper 450 db, and 52% to the upper 200 db. Thus, it is reasonable to assume that these XBT data accurately reflect most of the upper ocean variability, and that even the casts which did not reach the nominal sampling depth provide useful information.

In order to fill data-sparse regions in 1979–81, an XBT dataset collected by the National Marine Fisheries Service (NMFS) was added to the Noumea set. A total of 3087 NMFS casts were added on the CP track. Comparison of isotherm depths during the interval of data overlap shows that there was no systematic offset between the two datasets and less than 1% data duplication. Casts of dubious quality were removed by plotting each profile and visually comparing it with nearby (in space or time) profiles. This procedure was preferable to an objective rejection criterion based on multiples of the sample root-mean-square since the dataset includes large changes associated with the El Niño of 1982–83. For example, the rms of temperature at the equator at depths above 200 m for the entire six-year period of observation is more than twice that for the pre-El Niño period. An objective criterion based on rms would either be too lax if the entire six years of data were used or too severe if just the pre-El Niño

rms were considered. Approximately 2% of the Noumea dataset and 10% of the NMFS dataset were rejected by the subjective rejection criteria.

After quality control, the irregularly spaced casts were gridded in latitude, depth and time in order to obtain a uniform, complete matrix from which to estimate zonal geostrophic transports. To construct this three-dimensional grid, the casts were first grouped into 41 1° latitude bands centered on integer latitudes from 20°N to 20°S. The longitudes of casts within the section boundaries were ignored. In each latitude band the temperatures were gridded as a function of depth and time by an objective interpolation scheme (Laplacian method). The grid spacings were one month and 5 m depth. These 41 grids were merged to form a three-dimensional grid of temperature as a function of latitude, depth and time. The gridded values were then smoothed in latitude by a ¼–½–¼ filter to reduce the small-scale noise. Alternatively, the casts might have been gridded first in latitude and depth by constructing monthly meridional sections and then merging these. However, this technique would involve interpolation in latitude across major hydrographic features in regions of sparse data, which unnecessarily obscures structures known to exist. The present method allows interpolation in time only at each particular location.

For the purposes of this study, the observations were considered to lie along a quasi-meridional section. In order to retain as much information as possible, the section is constructed in two offset blocks, with meridional boundaries at 150° and 170°W north of 5°N and 180° and 160°W south of the equator and with sloping boundaries between the two blocks (Fig. 1). Since neither the ship track nor the pressure gradient lies along a meridian, systematic errors are introduced by considering the track to be meridional.

In the calculations reported here the zonal geostrophic speed is estimated to be proportional to the pressure change (Δp) per meridional distance along the track (Δy), where Δp and Δy are shown in Fig. 2. If u'

denotes the zonal speed obtained by this method and u the true zonal component of the geostrophic velocity, then

$$u' = u(1 + \tan\gamma \tan\theta),$$

where γ is the angle of the pressure gradient with a meridian and θ is the angle of the ship track with a meridian (Fig. 2). If either γ or θ were zero, there would be no error. The ship track runs from about 20°S, 180° to 20°N, 150°W, so $\tan\theta$ is approximately 0.75. The track splits north of the equator, with the western leg going to Hawaii and the eastern leg to the U.S. west coast (Fig. 1). The meridional geostrophic velocity is calculated between these two legs, and $\tan\gamma$ is estimated from the ratio of meridional to zonal velocities,

$$\tan\gamma = -\frac{v}{u} = -(1 + \tan\gamma \tan\theta)\frac{v}{u'}$$

$$= -[(u'/v) + \tan\theta]^{-1}.$$

The time-average meridional velocity over 5° to 10°N is -1.0 cm s^{-1}, while the average zonal velocity (u') is $+19.5$ cm s^{-1} in the same region (North Equatorial Countercurrent). Thus, $\tan\gamma$ is about $+0.05$ ($\gamma = 183°$), and the average zonal speed in the Countercurrent is overestimated by 4%. In the region from 10° to 19°N (North Equatorial Current) the average meridional velocity is -1.67 cm s^{-1} and the zonal velocity average is -9.5 cm s^{-1}. Here $\tan\gamma$ is about -0.16 ($\gamma = -9°$) and the average zonal speed in the North Equatorial Current is underestimated by 12%.

Wind stresses derived from satellite observations (Sadler and Kilonsky, 1985) are used in section 6 to compute Ekman pumping. These wind stresses are estimated from low-level cloud motions observed from geostationary satellites and brought down to the surface by a model utilizing the climatological mean shear between the surface and the cloud level. The stress values are given in units of meters squared per second squared (psuedostress); these were converted to units of force per area using a value of 1.2 kg m^{-3} for the density of air at the sea surface and a constant drag coefficient of 1.5×10^{-3} and averaged over the 20° longitude width of the ship track. Of the two components of the curl, $\partial\tau^x/\partial y$ is in almost every case the dominant term; its average magnitude on the CP track is more than seven times the magnitude of $\partial\tau^y/\partial x$. All of the calculations reported in section 6 were also performed using the Florida State University wind product derived from ship wind observations (Goldenberg and O'Brien, 1981). The same conclusions would be drawn from the FSU data as from the Sadler product.

3. Calculation of dynamic height

A mean T–S relation, in 2° latitude bands, was constructed from CTD data collected between March 1979 and March 1980 on the Hawaii–Tahiti Shuttle, averaging across the three meridional sections (150°, 153°
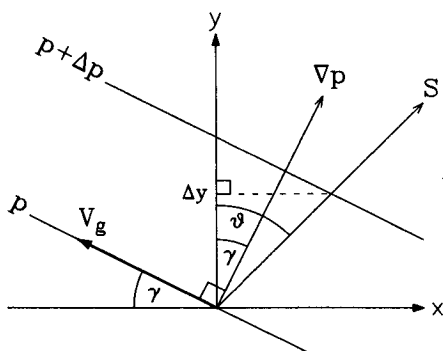

FIG. 2. Schematic diagram showing the ship track (S) tilted an angle θ from a meridian and the pressure gradient (∇p) tilted an angle γ from a meridian. x and y are the zonal and meridional directions and V_g is the geostrophic velocity vector.
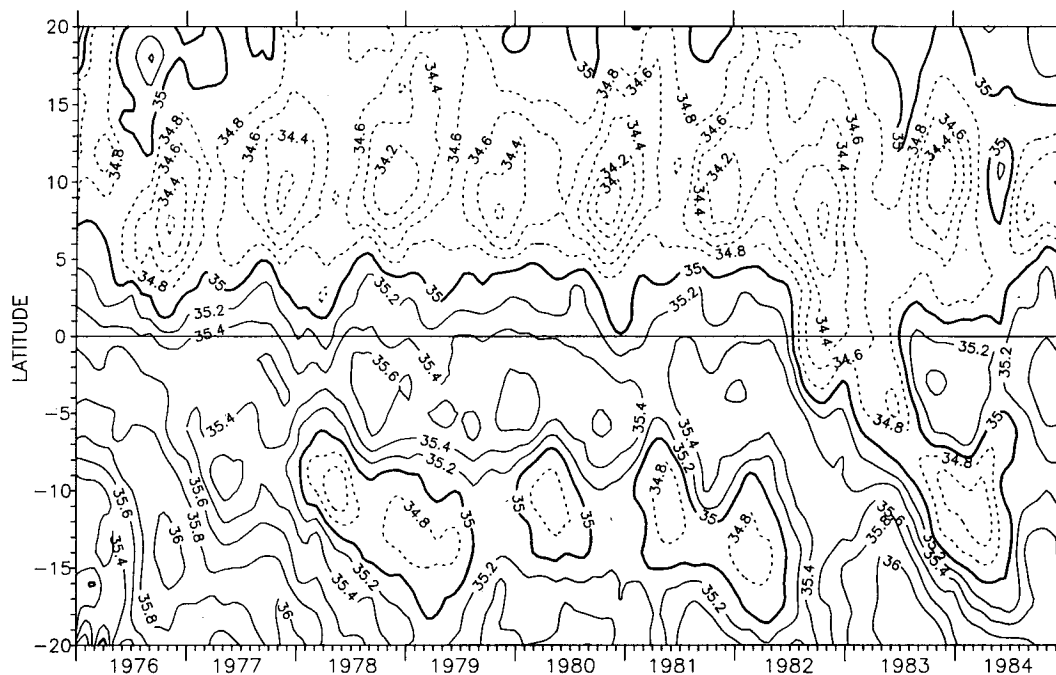
FIG. 3. Surface salinity on the CP track. The contour interval is 0.2, and dashed contours indicate salinity lower than 35.

and 158°W). In the Northern Hemisphere, the Shuttle track closely approximates the CP XBT lines; however, in the Southern Hemisphere the two tracks diverge and are as much as 25° longitude apart. Emery and Dewar's (1982) and Emery and Wert's (1976) analyses of the mean $T-S$ relation in the Pacific indicate that this longitudinal difference is not important in the calculation of dynamic height. In order to check the representativeness of the Shuttle $T-S$, dynamic height calculations from the XBT data (using the technique described below) were compared using two other sources of $T-S$ information: (i) Emery and Dewar (1982) and (ii) ORSTOM (Noumea) files for 1956–83. In no case did the differences in dynamic height among the three datasets exceed 2 dyn cm (1 dyn cm = 10 m² s⁻²). The differences are roughly equivalent to the noise introduced by internal waves; for example, Hayes (1982) estimated the internal wave contribution to be 1.1 dyn cm at the equator in the eastern Pacific.

It must be pointed out that the three $T-S$ relations which were compared do not contain entirely independent information; for example, the ORSTOM files contain the Shuttle data and possibly much of the same data as does the Emery and Dewar (1982) mean $T-S$. A further caution is that we have little data on deep salinity fluctuations during El Niño events such as occurred during 1982–83. A single CTD cast (R/V *Discoverer* at 0°, 155°W) constitutes the only CP subsurface salinity information obtained during the 1982–83 event (Fig. 5). It shows a $T-S$ correlation below 25°C which is very close to the mean Shuttle relation.

For the calculation of dynamic height, salinity[1] throughout the mixed layer must be estimated. In the CP, surface salinities change appreciably on annual and interannual time scales and are not well correlated with surface temperature, so the use of a mean $T-S$ relation in the surface layer is not justified. Figure 3 shows the sea surface salinity (SSS) measured by the ship of opportunity network over the period 1976 through 1984. In Fig. 3, a prominent annual signal of low SSS at about 10°N occurs in the second half of each year. Near 10°S, a similar annual signal of low SSS is also present.

In both regions, the seasonal pattern of precipitation deduced from seasonal means of outgoing longwave radiation (OLR) (Leibmann and Hartmann, 1982) corresponds well to the timing of the low SSS signals. However, it is not possible to estimate accurately the amounts of precipitation from the OLR data, and island rainfall records are scattered and contaminated by orographic effects. In addition, it is shown in section 4 that the North and South Equatorial countercurrents vary seasonally and are strongest at the time of year when the SSS is decreasing in their respective regions. Since both currents flow eastward from regions of lower

SSS, it is likely that advection also contributes to the annual freshening seen in Fig. 3, but it has not been possible to quantitatively show this by budget calculations. It can only be concluded that both processes probably play a role in the annual lowering of SSS.

For the purpose of computing dynamic height, these SSS signals are not large sources of variability. The peak-to-peak SSS variation is less than 0.5 (Fig. 3). If the SSS represents the salinity of the entire (relatively shallow) mixed layer, the effect of this variability on the dynamic height is about 2 dyn cm, which is relatively small in these regions where the annual dynamic height variation is on the order of 10 dyn cm.

During the 1982–83 El Niño, on the other hand, the surface salinity fluctuations made a significant contribution to the dynamic height variability near the equator. Prior to the El Niño, equatorial SSS variability was low, with an rms of 0.17 (Fig. 3). In July–August 1982, surface salinity fell rapidly and remained low for a year, gradually recovering by late 1983. The most intense SSS anomalies (approximately −1) are within 5° of the equator, where even small meridional pressure gradients are significant.

The equatorial thermocline during the last half of 1982 was at the second deepest level observed in the six-year period of measurement (Fig. 4). At this time the upper layer was very nearly isothermal, with no more than 0.2°C change over nearly 100 m. If the salinity were similarly uniform, a salinity decrease of 1 in the 100 m upper layer would produce a dynamic height increase of about 7 dyn cm. This increase is

significant compared with the pre–El Niño rms dynamic height of 3 dyn cm at the equator. On the other hand, if the SSS value represents only a thin fresh surface layer, it would not have a large effect on the dynamic height.

Visual inspection of CP $T(z)$ and $S(z)$ profiles suggests that even with low SSS, the depth of the halocline (if there is one) usually corresponds closely to the depth of the thermocline. Counterexamples exist of strong salinity gradients above the main thermocline (for example, in the western Pacific after the El Niño of 1965–66), but even in these cases the halocline is located in a weak temperature gradient between two uniform layers (Rotschi et al., 1972). It does not seem likely that a strong salt gradient could exist for long in a layer of uniform temperatures in the open ocean. A strong halocline would be a stable layer inhibiting the vertical mixing of heat; thus, a temperature gradient would form there due to heating from above and mixing above and below the halocline. Since only an isothermal layer was observed down to the thermocline during the period of low SSS in late 1982, it is presumed that there were not strong vertical salinity gradients in the upper layer during this period. The magnitude of the local rainfall also suggests that the low salinity extends throughout the isothermal layer, since without a deep isohaline layer the extreme local (and regional) precipitation would produce a much lower SSS (see discussion in section 5). The only observation of the subsurface salinity in the low SSS water mass of 1982–83 in the CP shows a constant salinity over the upper 60 m, with
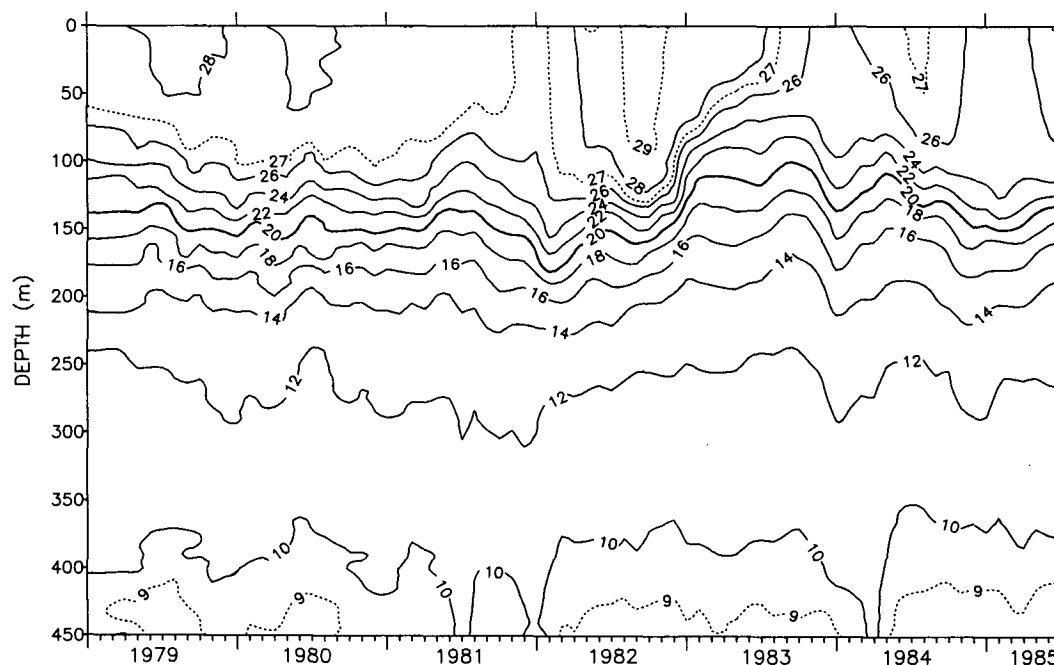

FIG. 4. Depth–time plot of temperature (°C) at the equator on the CP track. Contour interval is 2°C with supplemental (dashed) contours at 9°, 27° and 29°C.

a halocline right at the top of the thermocline (Fig. 5). This profile is in agreement with the assumption that temperature and salinity are both uniform above the thermocline.

In order to estimate the salinity for the density calculation, it is assumed that above the center of the thermocline salinity and temperature have exactly the same proportional vertical gradient structure. Within and below the thermocline the salinity profile is represented by the mean T–S relation from the Hawaii–Tahiti Shuttle. At each latitude an isotherm is chosen that is near the top of, but always within, the thermocline. For example, at the equator 25°C is chosen (Fig. 4). Below this isotherm the mean T–S is used to estimate the salinity in the usual way. At higher temperatures, the assumed T–S relation is a linear connection, on T–S coordinates, between the mean T–S at the chosen isotherm and the known SST and SSS. The linear connection effectively defines an isohaline layer where the temperature is isothermal and a halocline at the top of the thermocline. This scheme tailors the T–S relation to the conditions at each position and time, using the mean T–S (a function of latitude) below the thermocline and the known SSS and SST (functions of latitude and time) above. All of the computations of dynamic height reported here use this method, which will be referred to as the "Linear T–S Scheme" (LTS). Dynamic heights were computed relative to 450 m (Fig. 6).
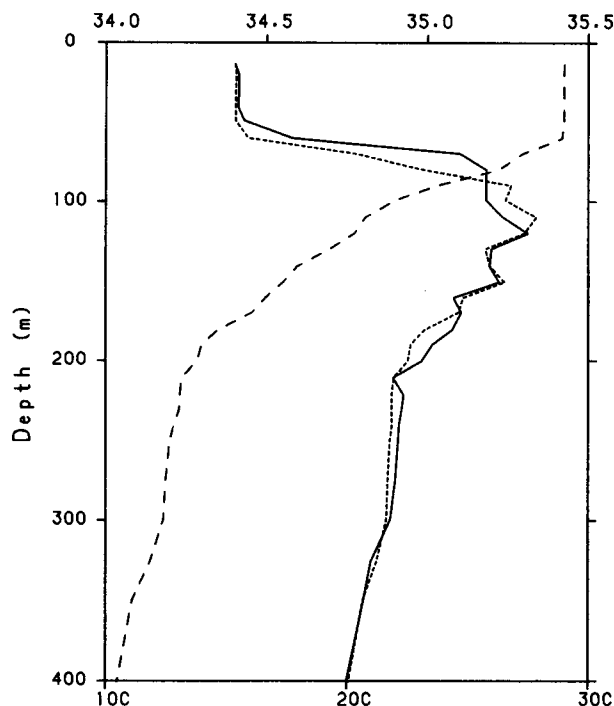

FIG. 5. Temperature (long dashes) and salinity (solid line) measured by CTD from R/V *Discoverer* on 9 April 1983 at 0°, 155°W. Salinity hindcast using the linear T–S scheme is shown by short dashes.

The LTS was tested by comparison with three independent sources of density information: first, with dynamic height computed from the CTD data of the Hawaii–Tahiti Shuttle; second, with dynamic height measured by the single *Discoverer* CTD cast in April 1983; and third, with a sea level index (Wyrtki, 1974a,b). In the first comparison 0/400 db dynamic height was calculated from 979 Hawaii–Tahiti Shuttle CTD casts (all casts from Shuttle legs 2 through 14) in three ways: (i) using the measured salinity in the usual way (which was considered to be the "true" dynamic height), (ii) using the LTS, and (iii) using only the mean T–S (which was constructed from the Shuttle data itself). Differences between the two estimates and the "true" values were calculated. The rms difference for the LTS was 0.91 dyn cm, with a maximum error of +3.3 dyn cm, whereas for the mean T–S the rms difference was 1.25 dyn cm with a maximum error of −4.8 dyn cm. The mean error due to the LTS was +0.19 dyn cm, indicating a slight low-salinity bias. Figure 7 shows the distribution of the errors using the LTS. Since the mean T–S used was derived from the Shuttle data itself, a further check is provided by repeating this hindcasting calculation using the Emery and Dewar (1982) T–S curves. Here the LTS rms difference was 1.43 dyn cm, and for the mean T–S, the rms difference was 2.27 dyn cm, about 60% larger. The latter figure agrees with an Emery and Dewar (1982) estimate of 2.3 dyn cm rms difference in the same region using their mean T–S. The LTS is significantly better than a mean T–S scheme for the hindcast of the Shuttle salinities, and with large variations of upper layer salinity, the improvement will be even more pronounced.

Comparison of the R/V *Discoverer* salinity profile and LTS hindcast is shown in Fig. 5. The LTS reproduces the measured salinity nearly exactly. Dynamic height relative to 400 db was calculated from this cast using the salinity profile reconstructed by the LTS and the CTD-measured salinity profile. The difference was 0.62 dyn cm (LTS higher than CTD), with 0.1 dyn cm of the difference occurring below the thermocline in the mean T–S region and 0.52 dyn cm in the linear T–S region. As a further comparison, the dynamic height was calculated using the mean T–S extended to the surface, as would be done if there were no SSS information; this procedure resulted in a 3.58 dyn cm error (mean T–S lower than CTD), which is due to the neglect in this case of the anomalously fresh water in the upper 60 m. It is noted that there is no evidence in this cast of subthermocline salinity anomalies; the largest salinity difference from the mean T–S below 200 m was 0.037.

Finally, dynamic height at the equator computed using the LTS is compared to an index of equatorial sea level (Wyrtki, 1974a,b) shown in Fig. 8. The index is derived from sea level at Christmas Island (1°57′N, 157°W) and Canton Island (2°48′S, 171°W). Before
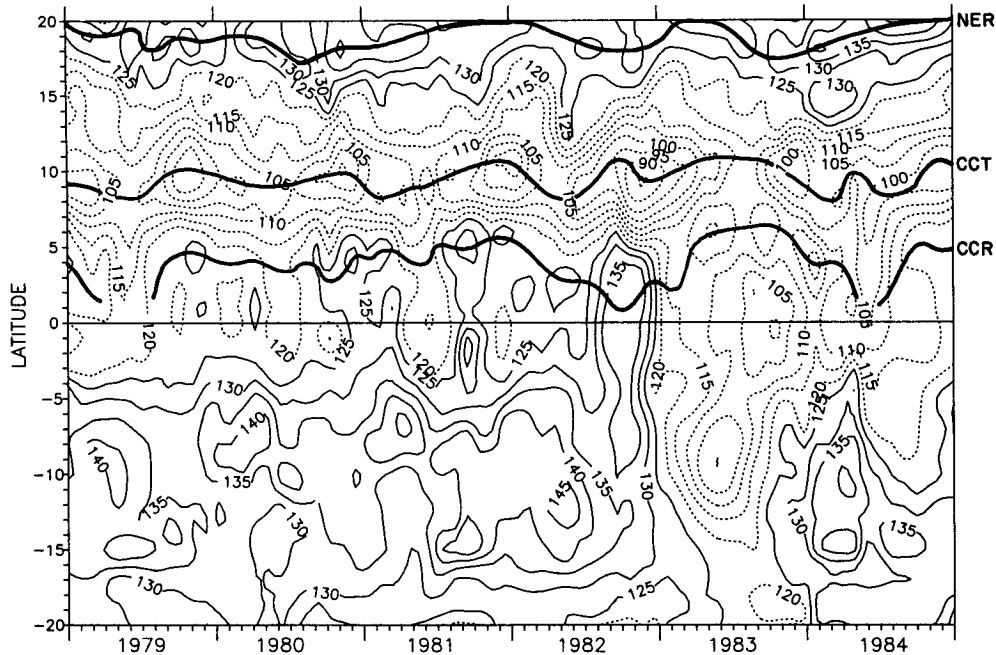
FIG. 6. Latitude–time plot of dynamic height (dyn cm) relative to 450 m on the CP track. Contour interval is 5 dyn cm and contours less than 125 dyn cm are dashed. The North Equatorial Ridge (NER), Countercurrent Trough (CCT) and Countercurrent Ridge (CCR) are shown by heavy lines.

the 1982–83 El Niño event, dynamic heights computed using the LTS and mean T–S were nearly identical (Fig. 8), reflecting the low variability of SSS during this period. The pre–El Niño correlation of dynamic height at the equator with the sea level index was 0.53. In August 1982, sea level rose 15 cm. The LTS dynamic height rise was 14 dyn cm in September, similar in timing and magnitude to the sea level signal, but comparable dynamic height calculated using the mean T–S rose only 8 dyn cm (Fig. 8). This comparison shows that salinity variations can be dynamically significant in these extreme conditions and must be taken into account in the estimation of dynamic height.

4. Pre–El Niño annual variations

a. Temperature variations

It is useful to visualize the thermocline fluctuations associated with variations in the major zonal currents before considering the geostrophic transports. The pre–El Niño period (January 1979 to July 1982) is considered separately since large changes associated with the El Niño of 1982–83 occurred over nearly the entire CP track region, beginning in August 1982 (see section 5). Figure 9 shows the mean temperature section on the CP track during the pre–El Niño period. For later reference, the major geostrophic currents that can be inferred from this temperature section (shown directly in Fig. 10) are the westward North Equatorial Current (NEC) (10°–19°N), the eastward North Equatorial Countercurrent (NECC) (4°–10°N), the westward

South Equatorial Current (SEC) (15°S–4°N), and the intermittent eastward South Equatorial Countercurrent (SECC) (8°–12°S). The eastward North and South Subsurface countercurrents (NSCC, SSCC) are associated with the poleward rise of the 10°C isotherm at 2° to 4°N(S). In addition, the eastward Equatorial Un-
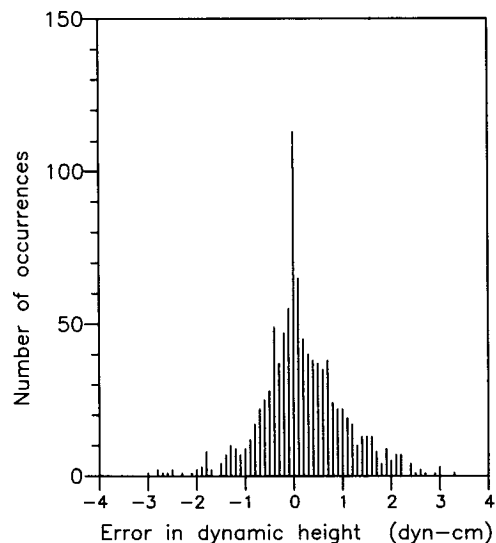

FIG. 7. Frequency distribution of differences between dynamic heights relative to 400 m calculated from measured salinity (CTD) and hindcast salinity (LTS scheme) for 979 Hawaii–Tahiti Shuttle CTD casts.
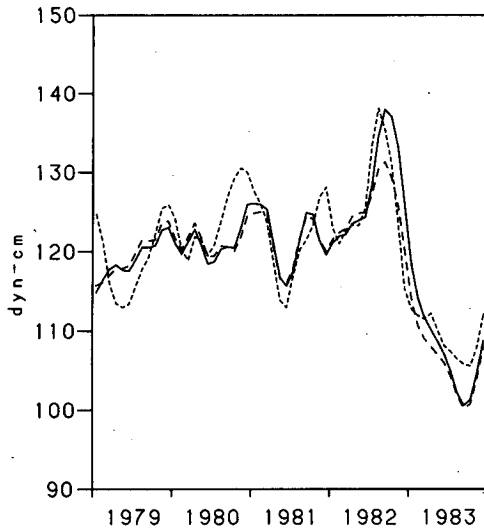
FIG. 8. Comparison of dynamic height (dyn cm) at the equator calculated from the linear T-S scheme (solid line) and from a mean T-S alone (long dashes) and an index of equatorial sea level (cm) (short dashes). Dynamic heights are relative to 450 m; sea level reference level is arbitrary.

dercurrent (EUC) can be inferred geostrophically from the troughing of the 12° and 14°C isotherms and the westward Equatorial Intermediate Current from the ridging of the 10°C isotherm across the equator.

Previous studies (Kendall, 1970; Meyers, 1979) have pointed out that in the tropical Pacific the thermal structure is approximated well by a two-layer system, particularly in the Northern Hemisphere where the thermocline is sharp. Empirical Orthogonal Function (EOF) analysis of the depth fluctuations of the 14°, 20° and 24°C isotherms, which approximately span the strong vertical temperature gradient, shows that the movements of all three of these isotherms are strongly in phase and have similar amplitudes; thus the motion of the 20°C isotherm is a good proxy for overall thermocline motion. It is shown below that transports of the NECC and NEC derived from the two-layer assumption, using the motion of the 20°C isotherm to represent interfacial movement, give a good estimate of geostrophic volume transport.

Figures 11a and 11b show the depth of the 20°C isotherm on the CP track during 1979-84. Before the massive changes associated with the El Niño that began in 1982, the largest variability in 20°C depth (rms greater than 10 m) was found between 10° and 17°N, between 10° and 15°S, and near 5°N. This variability is primarily associated with annual fluctuations in the NEC, NECC and SECC. In order to visualize these changes, the field of 20°C depth was decomposed into EOFs (Figs. 12 and 13). The EOF decomposition brings out the seasonal cycles and provides a clear picture of the variability. It is emphasized that the EOFs have no dynamical significance; the technique is used solely as
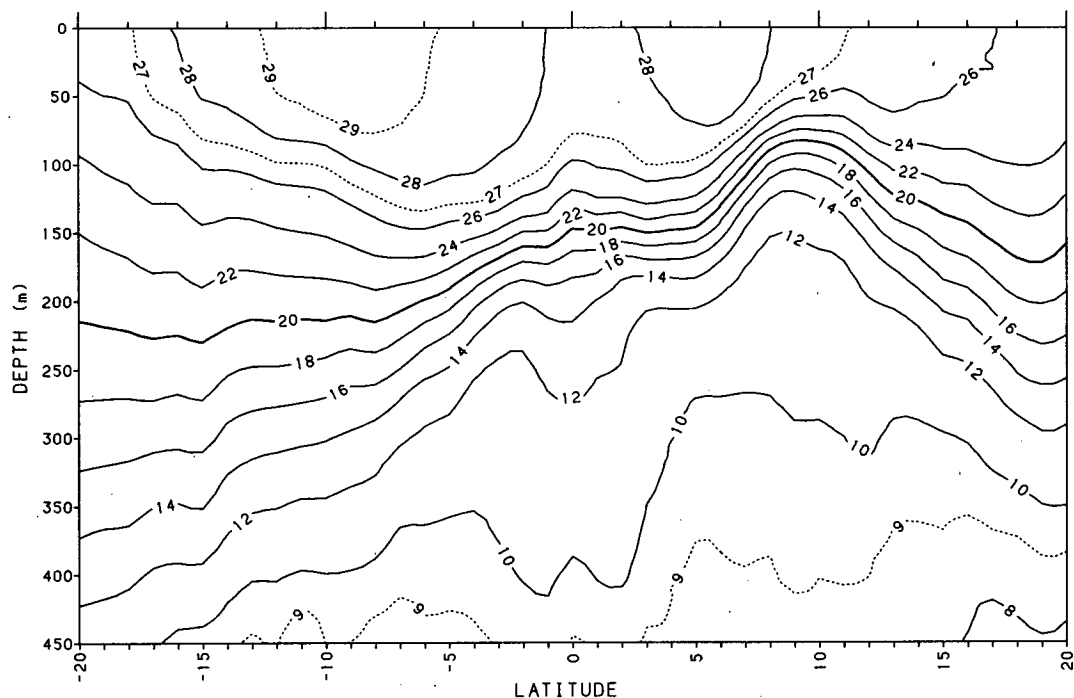

FIG. 9. Mean temperature (°C) on the CP track for the pre-El Niño period (January 1979 through July 1982). Contour interval is 2°C with supplemental (dashed) contours at 9°, 27° and 29°C. The slope break in the thermocline near 4°N marks the southern boundary of the NECC.
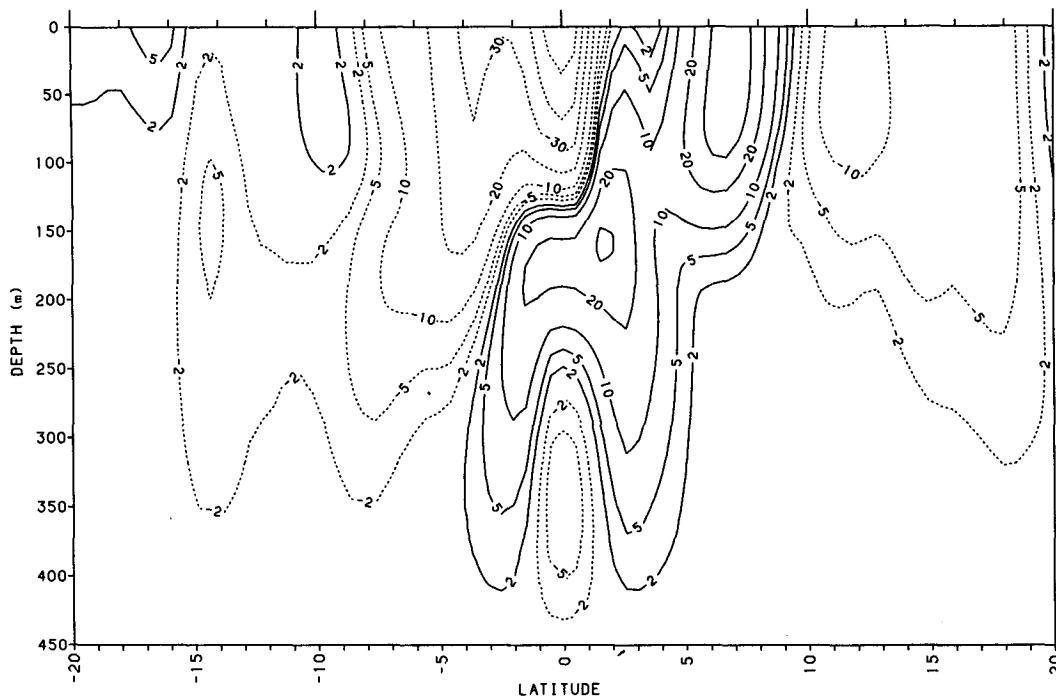
/

FIG. 10. Mean zonal geostrophic velocity (cm s⁻¹) relative to 450 m on the CP track for the pre-El Niño period (January 1979 to July 1982). Contours are ±2, 5, 10, 20, 30, 40 and 50 cm s⁻¹. Dashed contours indicate westward flow. The southern boundary of the NECC is shown by a heavy dashed line.

a convenient means of visualizing and quantifying signals with coherent large-scale variation. EOF 1 (Fig. 12) represents 38% of the total variance and 60% to 70% of the variance in the regions 1° to 6°N and 10° to 14°N. The major signal, which is clearly visible in Fig. 11a (bottom panel) as well, is an out-of-phase annual oscillation of the isotherm ridge near 10°N and the trough near 4°N. In the middle part of each year, the ridge is low and the trough high, implying a weak pressure gradient across the NECC; at the end of the year, the opposite regime prevails with a strong thermocline slope across the Countercurrent. The peak-to-peak variation of ridge–trough depth difference is about 40 m; the mean ridge–trough difference is about 60 m (Fig. 9). In addition, EOF 1 shows that the thermocline over most of the NEC region (from 10° to about 18°N) fluctuates synchronously with the isotherm ridge near 10°N.

EOF 1 suggests that coherent fluctuations of the thermocline over the equatorial waveguide region (5°S to 5°N) have a significant annual component of variability. This is borne out by the depth of 20°C with the 12-month running mean (Fig. 11a, middle panel) removed, which shows a fairly regular annual equatorial cycle of high (low) thermocline in the middle (end) of each year (Fig. 11a, bottom panel). EOF 1 shows that annual fluctuations of 20°C depth from 5°N to 5°S represent about 40% to 70% of the variance in that region (higher in the north). The pressure gradient

across the NECC is partly controlled by the depth of the thermocline at the trough near 4°N; the coherent fluctuation of the waveguide region (see also Fig. 24) indicates that a portion of NECC variability is governed by the distinct dynamics of the equatorial waveguide.

EOF 2 (Fig. 13) represents 16% of the total variance and 50% to 60% of the variance near 5° and 15°S. The mean depth of 20°C is nearly flat at about 210 m from 7° to 20°S (Fig. 9), with mean westward shear below and eastward shear above. EOF 2 is also predominantly annual and depicts an out-of-phase oscillation across the region of the SECC. The main signal is an upward (downward) motion of the thermocline near 15°S (6°S) near the turn of each year, tilting the thermocline down toward the equator and implying increased eastward geostrophic flow (the SECC) in the early months of the year. The peak-to-peak variation of depth difference across the current is about 25 m. Figure 11a (bottom) and Fig. 24 show that the phase of the annual fluctuation near 15°S is shifted about three months compared with the fluctuation in the Northern Hemisphere spanning the equator; thus the EOF decomposition puts this variability in a second EOF. These two EOFs show that about 50% of the total variance in thermocline depth on the CP track is at the annual period.

b. Zonal geostrophic transports

Geostrophic zonal velocities were estimated by differencing the dynamic height grid; Fig. 14 shows the
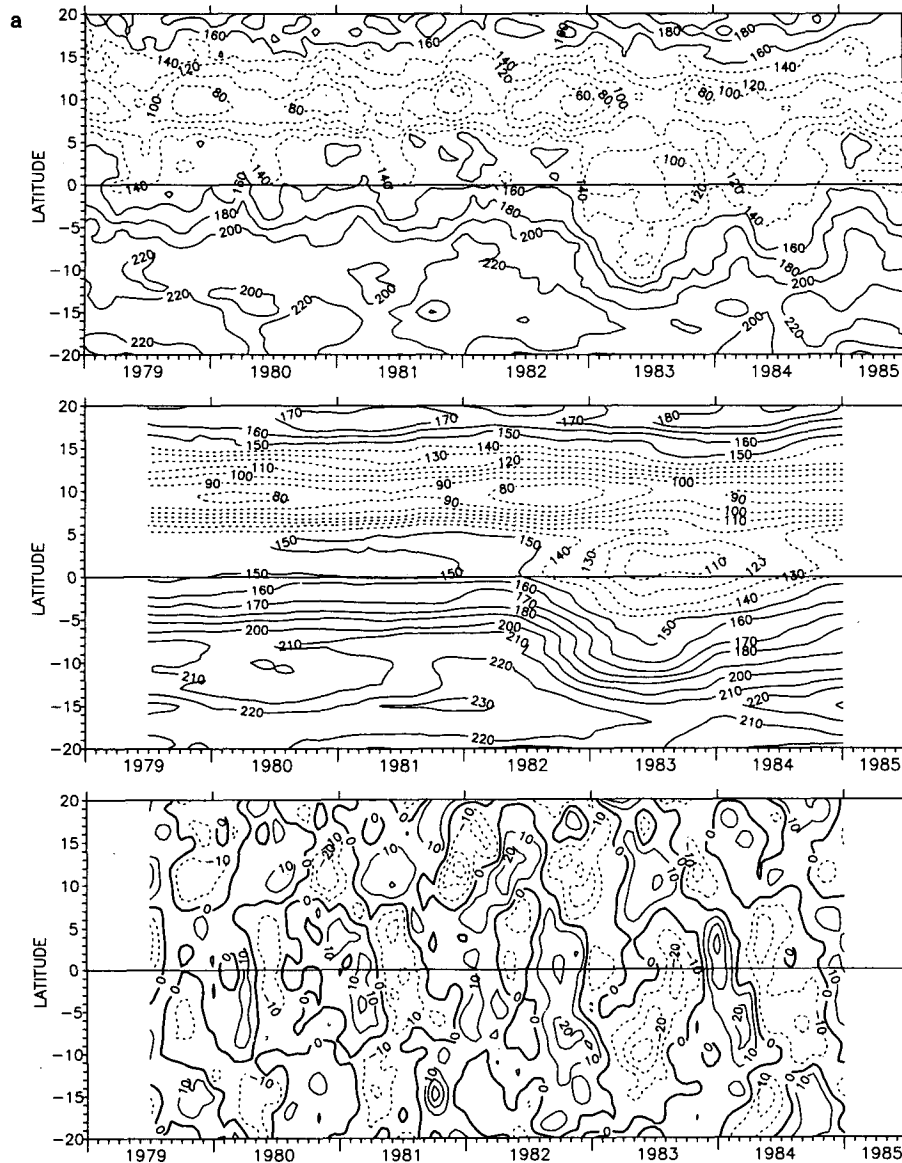
FIG. 11a. Latitude–time plots of the depth (m) of the 20°C isotherm on the CP track: (top panel) raw depths, (middle panel) 12-month running mean, and (bottom panel) depths demeaned by the 12-month running mean (top minus middle).

surface zonal flow and Fig. 10 shows the mean geostrophic flow during the pre–El Niño period. A second difference was taken from the dynamic heights at 1°N, 0° and 1°S, to compute the geostrophic velocity at the equator (Lukas and Firing, 1984). The mean geostrophic flows near the equator determined by this method (Fig. 10) show EUC speeds that are only about one-fourth as large as that found in other studies (Lukas and Firing, 1984; Wyrtki and Kilonsky, 1984), and the EUC is found about 50 m too deep. In addition, the equatorial geostrophic flow indicates large and probably unrealistically rapid fluctuations (Lukas and Firing, 1984). These results may be attributable partly to the

gridding process, in which the longitudinal position of each XBT profile within the section boundaries was ignored. Hayes (1982) also showed that the signal-to-noise ratio of monthly dynamic height was low near the equator at 110°W due to small-scale high-frequency fluctuations. In light of these problems, geostrophic speeds within 2° of the equator were not used in computing transports.

Transports were computed by plotting the estimated zonal flow field and determining the boundaries of the currents for each individual month, then integrating over the area of the current. Criteria for determination of the current boundaries are described below. Except
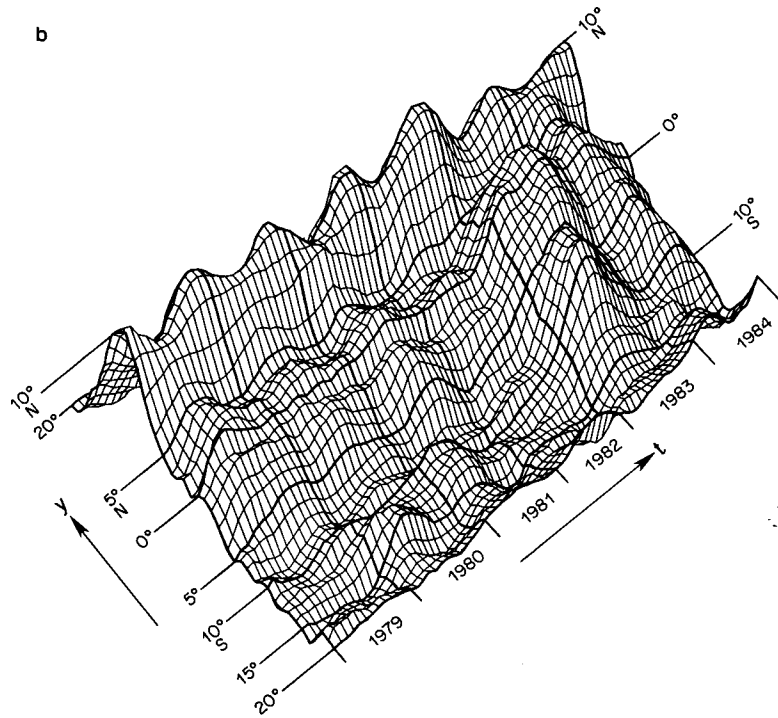
b

FIG. 11b. Raw depths of the 20°C isotherm.

as noted, speeds less than 2 cm s⁻¹ have been excluded from the transports (Wyrtki and Kilonsky, 1984).

1) NORTH EQUATORIAL CURRENT

The NEC was defined as all flow above 200 m between the southern boundary of westward surface flow near 10°N and the northern boundary near 19°N, plus all westward flow greater than 2 cm s⁻¹ below 200 m in this latitude range. There was no difficulty in determining the surface boundaries, which were clearly defined during the entire period. Eastward flow above 200 m was included since the NEC frequently contains mesoscale eddies in the region near 15°N (Wyrtki, 1982) and excluding just the eastward part of these would inflate the transport. However, the eastward

transport in the NEC never exceeded 0.5 Sv (1 Sv = 10^6 m^3 s^{-1}) in any month. Westward flow greater than 2 cm s^{-1} below 200 m was included since the NEC extends to at least 300 m near its poleward edge (Fig. 10). Excluded transport due to speeds less than 2 cm s^{-1} averaged less than 1 Sv. It is possible that the reference level of 450 m used here is too shallow to include the entire NEC (Wyrtki and Kilonsky, 1984). During the Hawaii-Tahiti Shuttle, mean (rms) geostrophic speeds at 450 m relative to 1000 m below the NEC were −0.6 cm s^{-1} (2.6 cm s^{-1}). This mean speed is equivalent to a volume transport of 2.7 Sv, integrated over 450 m and the width of the NEC.

Figure 14 shows NEC surface velocities of 10 to 20 cm s^{-1} near the southern edge of the current at about 10°N, a region of weaker and variable flow averaging
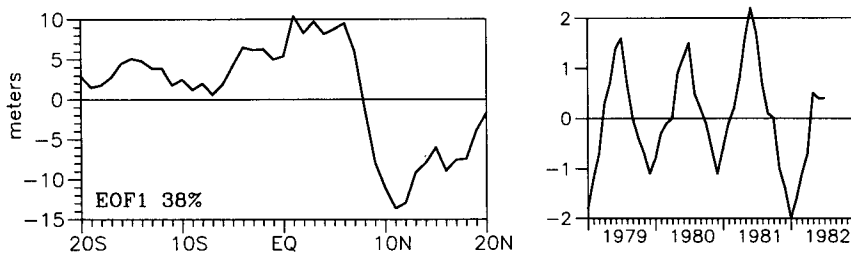

FIG. 12. EOF 1 of the depth (m) of the 20°C isotherm on the CP track, representing 38.2% of the variance. The time amplitude function is dimensionless.
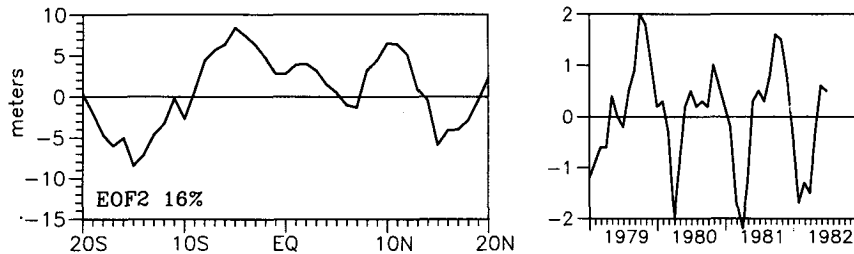
FIG. 13. As in Fig. 12 except for EOF 2, representing 15.8% of the variance.

about 5 cm s^{-1} near 14°N, and a second maximum of surface velocity near 16°N with speeds of 8–10 cm s^{-1}. Meyers (1975) and Wyrtki and Kilonsky (1984) also found the highest speeds near the southern edge of the current. The main ship of opportunity track (into Honolulu) is in the lee of the islands of Hawaii and Maui north of 19°N. Patzert (1969) found that eddies (~100 km diameter) are common in the lee region due to winds blowing through the high mountains of the islands. It is likely that the estimates of NEC velocities reported here are questionable at the northern end of the ship track and that NEC transports are underestimated compared to the NEC upstream of Hawaii. Seckel (1975) showed that the NEC at 148°W extended to about 23°N during 1964–65; however, speeds north of 20°N were generally less than 5 cm s^{-1}.

Figure 15 shows mean (rms) NEC transport of 19 Sv (1.7 Sv). A transport of 1 Sv is equivalent to 5 cm s^{-1} velocity in a layer 1° latitude wide and 200 m deep.

Since a dynamic height error of only 2 dyn cm, which is about the level of internal wave noise (Hayes, 1982), would give this geostrophic velocity (at 15°N), the signal-to-noise ratio of NEC geostrophic transport is low and the variation shown in Fig. 15 is near the limit of detectability. Wyrtki and Kilonsky (1984) found mean NEC transports relative to 1000 db of 24 Sv at 158°W, using the CTD data from the Hawaii–Tahiti Shuttle (1979–80). The northern end of the 158°W Shuttle section was also in the lee of the Hawaiian Islands. The difference of 25% between the calculations reported here and those of Wyrtki and Kilonsky (1984) may be due partly to the underestimation of NEC flow by about 12% associated with the deviation of the ship track from a meridian (see section 2). In addition, during the Hawaii–Tahiti Shuttle the mean geostrophic speeds at 450 m relative to 1000 m below the NEC indicate a contribution of 2.7 Sv (11% of total) to the volume transport of the NEC, which is not included here.
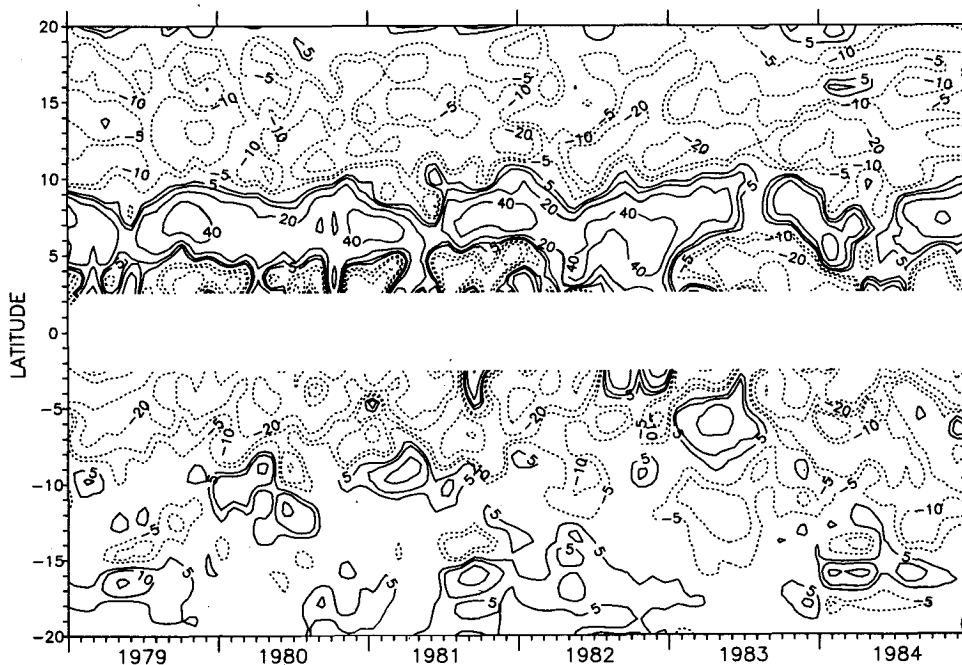

FIG. 14. Latitude–time plot of surface geostrophic velocity (cm s^{-1}) relative to 450 m. Dashed contours indicate westward velocity. Contours are ±5, 10, 20 and 40 cm s^{-1}.
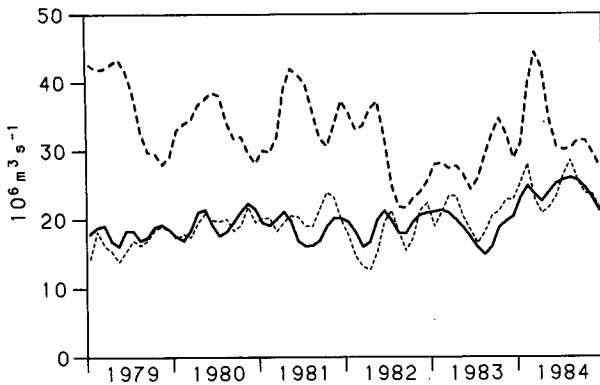
FIG. 15. Westward geostrophic volume transport relative to 450 m in the North Equatorial Current (solid line) and in the South Equatorial Current south of 2°S (heavy dashed line). NEC thermoclinic transport estimated using Eq. (1) is shown by short dashes.

FIG. 16. Dynamic height (dyn cm) relative to 450 m, averaged for the months April–May–June (solid line) and October–November–December (dashed line) over the years 1979 through 1981.

Meyers (1975) studied the variation of NEC transport between 11.5° and 20.5°N computed from monthly meridional Nansen bottle sections east of Hawaii during the TWZOS cruises in 1964 and 1965. Westward transport relative to 300 db in this region varied from a low of 11 Sv in February of both years to a high of 23 Sv in September 1964 (Meyers, 1975). Wyrtki (1974a), using the same dataset, noted that these transport fluctuations varied synchronously with the sea level difference (measured from island stations) across the current and concluded that the NEC has a large annual transport variation, being smallest in spring and largest in fall. These results seemingly contradict the very low transport variability reported here. Wyrtki (1982) noted that NEC transport variability during the Hawaii–Tahiti Shuttle was much lower than during 1964–65.

The discrepancy in the estimates of annual NEC variation may be an artifact of the sampling method. Figure 6 shows that the Countercurrent Trough (CCT) in dynamic height near 10°N, which is the southern boundary of the NEC, has an annual meander. It is observed near 8°N in the early to middle part of the year and near 10°N at the end of the year. Seasonal averages of dynamic height and zonal transport have been computed for the years 1979 through 1981 by averaging the data for the April–May–June (A–M–J) and October–November–December (O–N–D) seasons, which coincide with the extremes of annual variation of the NECC and NEC. The annual meander of the CCT is clearly seen in the seasonal average dynamic heights (Fig. 16). The mean volume transports for the same seasons (Fig. 17) show that much of the variability of the NEC also occurs near the southern edge of the current and that errors would result if the current were not measured all the way to the meandering CCT. In addition to an underestimation of mean transport, the annual fluctuation would be severely overestimated. Both the 1964–65 TWZOS sections (Meyers, 1975),
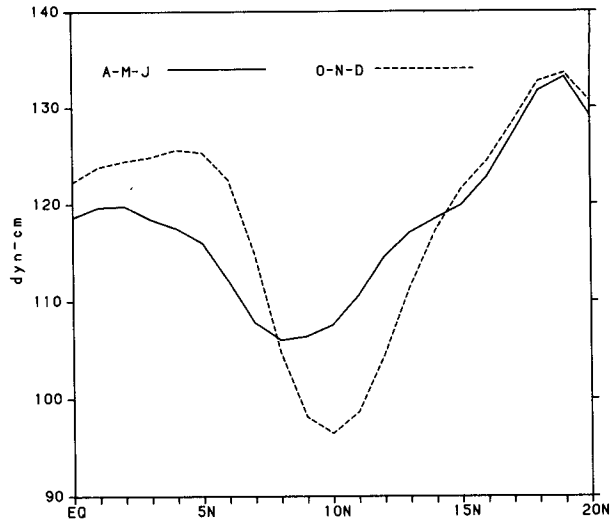
which extended only to 11.5°N, and the sea level index (Wyrtki, 1974a), which bases CCT depth on sea level at Kwajalein Island (9°N, 168°E), suffer from this problem. An index of the magnitude of the annual fluctuation is the percentage of total variance represented by the first annual harmonic. For NEC transport fluctuations, including the entire current, 13% of the total is in the first harmonic (Table 1). However, NEC transport poleward of 11.5°N, calculated from the XBT data to mimic the TWZOS latitude range, has a much more pronounced annual cycle; in this case 60% of the variance is at one cycle per year (Table 1). In both cases the phase of the first harmonic indicates maximum transport during late November to
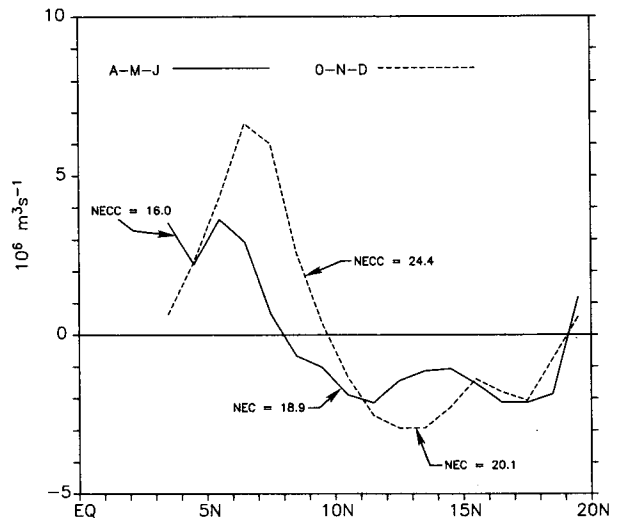

FIG. 17. Geostrophic volume transports relative to 450 m averaged as in Fig. 16. Totals for each current are indicated.

early December. The Hawaii–Tahiti Shuttle observations, which also show low NEC variability (Wyrtki, 1982), include the entire southern portion of the current.

Figure 16 shows that the surface pressure gradient across the NEC has significant annual variation, which is in apparent agreement with the earlier findings of strong annual variation of NEC transport (Meyers, 1975; Wyrtki, 1974a). Forty-three percent of the variance of dynamic height difference across the NEC is at one cycle per year (maximum gradient in November), yet the volume transport has only 13% of the variance at this frequency (Table 1). The relatively strong dynamic height fluctuation is also borne out by EOF 1 of 20°C isotherm depth (Fig. 12), which shows that in the southern region of the NEC the thermocline is deeper by 20–30 m during the A–M–J season. Two processes tend to counteract the pressure signal: first, the meander, in which the current is closest to the equator (hence a given pressure gradient implies a larger geostrophic speed) during the A–M–J season of weakest pressure gradient, and second, the deeper extent of the current (hence greater transport) at the same time of year. Neither of these effects is reflected in the surface pressure difference across the current. The relative strength of these effects can be conveniently studied using thermoclinic (two-layer) transports estimated using the depth of the 20°C isotherm (Wyrtki and Kendall, 1967; Kendall, 1970). The geostrophic transport in a two-layer fluid with the lower layer at rest is given by

$$U = -\left(\frac{g}{f}\right)\left(\frac{\Delta\rho}{\rho}\right)\Delta H \cdot \bar{H}, \qquad (1)$$

where U is the zonal volume transport, g the acceleration of gravity, $f = 2\Omega \sin\phi$ the Coriolis parameter, $\bar{H}$ the mean interface depth, ΔH the difference in interface depth between two locations, ρ the mean density, and $\Delta\rho$ the density difference between the two layers. Here $\Delta\rho/\rho$ has been chosen so that the 1979–81 mean thermoclinic transport agrees with that found by integrating the geostrophic velocity. In the case of the NEC this agreement was achieved by choosing $\Delta\rho/\rho = 5.7 \times 10^{-3}$. Transport was computed from (1) at each degree of latitude along the track, then integrated over the latitude range of each current for individual months. Figure 15 gives the resulting volume transport estimate for the NEC. Comparison of the integrated transport and thermoclinic estimate in Fig. 15 shows that the two-layer estimate gives a good representation of NEC transport; the correlation is 0.76. Eleven percent of the total variance of NEC thermoclinic transport is represented by the first annual harmonic, nearly the same as for the integrated transport (Table 1). In addition to being a simple method of estimating transport, the two-layer approximation is useful since it can be used to isolate the relative effects of the meander or

TABLE 1. Percentage of total variance represented by the first annual harmonic (amplitude of the first harmonic), 1979–81.

Variable	North Equatorial Current	North Equatorial Countercurrent
Dynamic height difference	39% (4.4 dyn cm)	76% (9.5 dyn cm)
Integrated volume transport	13% (0.8 Sv)	46% (5.7 Sv)
Two-layer transport	11% (1.1 Sv)	58% (6.4 Sv)
Two-layer transport; f set to 15° or 6°N	11% (1.3 Sv)	72% (7.5 Sv)
Two-layer transport; H set to 1979–81 mean	43% (2.5 Sv)	54% (5.7 Sv)
Integrated volume transport N of 11.5°N	60% (2.1 Sv)	

depth change of the current on the transport. This was accomplished first by choosing a fixed Coriolis parameter for the NEC and second by choosing $\bar{H}$ to be the 1979–81 mean at each latitude. The resulting transport estimates were compared with the two-layer estimate including the full variability of f and $\bar{H}$ (Fig. 15). In both cases the phase of the first harmonic indicated maximum transport in November. For the fixed Coriolis parameter (chosen to be at 15°N), the percentage of total variance in the first annual harmonic remained at 11% (Table 1), indicating that this effect is relatively minor in the case of the NEC. Fixing $\bar{H}$, on the other hand, led to an increase in the percentage of variance at one cycle per year to 43% (Table 1). This indicates that the annual depth variation of the current is about as important as the pressure difference variation in determining the transport, and that the two processes nearly cancel each other to produce the low variability observed. When all factors that affect NEC transport are taken into account, the annual transport variability is small.

2) NORTH EQUATORIAL COUNTERCURRENT

Boundaries of the NECC were more difficult to define than those of the NEC. The northern boundary, which coincides with the southern boundary of the NEC, was always clearly defined. However, in the south the NECC partly overlies and is connected with the deeper NSCC (Fig. 10), which also flows eastward. Since the two flows are governed by different dynamics (McPhaden, 1984), it is important to clearly distinguish between them. For the purpose of measuring geostrophic transport, the NECC was considered to be the flow dynamically associated with the thermocline slope from the ridge near 10°N to the slope break, or "elbow" in the thermocline near 4°N (Fig. 9). Eastward flow

below the thermocline or equatorward of the slope break was considered to be part of the NSCC and excluded from the NECC transport computation. The mean velocity section (Fig. 10) shows a velocity minimum between the two currents, which was used by Wyrtki and Kilonsky (1984) to distinguish the NECC from the NSCC. This minimum coincides with the thermocline slope break and was observable in nearly every month. A sloping boundary line at the velocity minimum was drawn for each month, and the transport integrated over the region poleward and upward of this line. Figure 10 shows the boundary for the mean velocity profile. This boundary was not necessarily the southernmost extent of eastward surface flow (for example, Fig. 10 shows that mean eastward geostrophic flow was observed to 2°N). However, eastward flow equatorward of the minimum generally was largest below the thermocline and had westward vertical shear above; i.e., it was not associated with the thermocline slope.

NECC transport is shown in Fig. 18, with a (pre–El Niño) mean (rms) of 21.1 Sv (5.7 Sv). The mean surface speed at the core of the current was 34 cm s^{-1}. Wyrtki and Kilonsky (1984) found mean NECC transport of 19.2 Sv relative to 1000 m during the Hawaii–Tahiti Shuttle. Average NECC transport for the comparable period derived from the XBT data is 19.9 Sv. The agreement between the two esimates suggests that the 450 m reference level is not a severe problem in estimating NECC transport. The NECC has significant annual variability, as expected from the fluctuations of surface dynamic height (Fig. 16) and EOF 1 of 20°C depth (Fig. 12). Similarly to the NEC, the dynamic height difference across the NECC varies much more than the transport, with 76% of the dynamic height variance represented by the first annual harmonic, while the transport has only 46% of its variance at that frequency (Table 1). This discrepancy is primarily due to the annual meander of the current, which is found
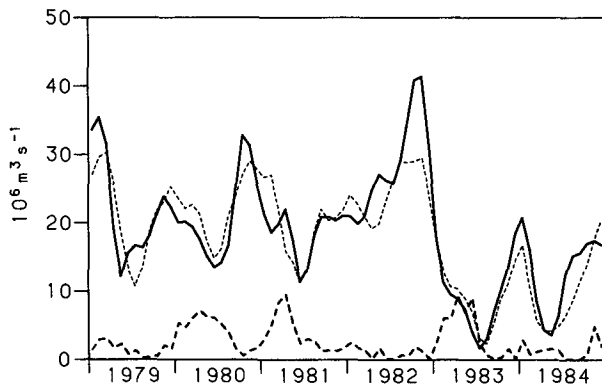

FIG. 18. Eastward geostrophic volume transport relative to 450 m in the North Equatorial Countercurrent (solid line) and the South Equatorial Countercurrent (heavy dashed line). NECC thermoclinic transport estimated using Eq. (1) is shown by short dashes.

closer to the equator at the time when the pressure gradient is weakest. The phases of all variables associated with the NECC indicate maximum flow in early December, nearly the same as for the NEC. Figure 16 shows the meander of the CCT near 10°N and the Countercurrent Ridge (CCR) near 4°N, which define the surface boundaries of the current, while Fig. 17 shows that the annual position of maximum flow is at 6°–7°N during the O–N–D season, when the dynamic height difference is largest, and near 5°N during the A–M–J season. The effect of the meridional shift of the current was studied using the thermoclinic transport, as in the case of the NEC. The correlation is 0.90 between the thermoclinic NECC transport and the transport computed from the integrated geostrophic velocity (Fig. 18). The mean integrated and thermoclinic transports were equal when $\Delta\rho/\rho$ was chosen to be 4×10^{-3}. Fifty-eight percent of the total variance of NECC thermoclinic transport is represented by the first harmonic (Table 1). When f is fixed at 6°N in (1) the annual cycle appears stronger, with 72% of the transport variance at one cycle per year (Table 1), about the same as for the dynamic height difference. The results indicate that the NECC meander substantially reduces the effect of the large pressure gradient fluctuation.

3) SOUTH EQUATORIAL CURRENT

The SEC spans the equator above the EUC and exists as a strong surface current south to about 8°S (Fig. 14); farther south it is found as a weak westward flow in the thermocline to at least 16°S (Fig. 10). In the region near 10°S the surface flow is variable and often eastward (SECC). The SEC was defined as all westward flow greater than 2 cm s^{-1} poleward of 2°S. Current velocities are strongest spanning the equator (Firing et al., 1981) and decrease to less than 5 cm s^{-1} by 10°S, so the highest speeds of the SEC are not included in the transport reported here. Using the data of Firing et al. (1981), Cantos-Figuerola and Taft (1983) find mean westward transport of 11 Sv in the SEC over 2°S to 2°N during the Hawaii–Tahiti Shuttle. The mean (pre–El Niño) SEC transport poleward of 2°S was 35.1 Sv, with a standard deviation of 5.1 Sv (Fig. 15). Cantos-Figuerola and Taft (1983) find comparable mean geostrophic SEC transport of 34 Sv within the same latitude limits during the Shuttle. Wyrtki and Kilonsky (1984) estimate SEC transport of about 40 Sv over the region 0° to 17°S during the Shuttle, using profiling current meter data between 2°S and the equator. Before 1982 the SEC had a strong annual cycle, with 54% of the total variance represented by the first annual harmonic. The phase of this harmonic indicates maximum flow in May, in agreement with Wyrtki (1974a), who finds that surface geostrophic flow in the SEC south of the equator is strongest from March to July and weakest from October to February. This annual variation is

nearly directly out of phase with the annual fluctuations of the NECC.

4) SOUTH EQUATORIAL COUNTERCURRENT

The SECC has been recognized in hydrographic and ship drift data for at least forty years (Reid, 1959, 1961). However, until recent times detailed study of its fluctuations has been difficult due to the lack of Southern Hemisphere data in the western and central tropical Pacific. Surface flow in the 8° to 20°S band is variable and often weak (Fig. 14), but there is a tendency for the occurrence of eastward flow at about 10°S (the SECC), a region of westward flow at about 15°S (SEC), and another region of eastward flow at the southern end of the section. The mean meridional temperature profile (Fig. 9) shows the eastward flows as two distinct areas of isotherms sloping up to the south. Wyrtki (1974c, Fig. 2) shows two separate ridges in 0/500 m dynamic height: (i) a ridge that extends across the entire basin from about 13°S, 170°E to 25°S, 85°W, defining the northern limit of the eastward flow which extends southward to the Antarctic Circumpolar Current, and (ii) a smaller ridge at about 8°S that extends from about 155°E to 175°W defining the northern boundary of the SECC. The above map indicates that the eastward flow observed at the southern edge of the CP track (Fig. 14) is not the SECC and also that the mean SECC is confined to the western South Pacific. Merle et al. (1969) observe two similar eastward flows at 170°E: the SECC at 5° to 10°S and a weaker flow, referred to as the South Tropical Countercurrent, which extends from about 15°S to the southern end of their section at 20°S and corresponds to the flow shown in Fig. 14 at the southern edge of the CP track. The Wyrtki (1974c) map indicates that this is the northern edge of the eastward flow on the poleward side of the southern gyre and not a countercurrent.

The SECC is defined as eastward flow greater than 2 cm s^{-1} between 5° and 15°S. In almost every month, SECC flow stronger than 5 cm s^{-1} was confined above 150 m, about the level of the 22°C isotherm, and was underlain by weak westward flow. Isotherms below 20°C continue to slope downward toward the south, at least as far as 20°S. During the Hawaii–Tahiti Shuttle, geostrophic speeds at 450 m relative to 1000 m at 8° to 12°S averaged −0.17 cm s^{-1}, which indicates that a 450 m reference level is appropriate. In Fig. 14, the SECC appears as four periods of eastward flow at about 10°S in the early part of 1979, 1980 and 1981 and at 6°S in early 1983. It was not present in 1982 or in 1984. The SECC was generally observed to occur as a single connected flow, in contrast to the observations of Eldin (1983), who found several branches in the SECC at 150°W during the Hawaii–Tahiti Shuttle. The depth of 20°C (Fig. 11) shows that the thermocline rose near 12°S and descended near 8°S in the early part of 1979, 1980 and 1981, but not in 1982 or 1983.

This annual cycle is also depicted in EOF 2 of 20°C depth (Fig. 13). The depth of 20°C with the 12 month running mean removed (Fig. 11a, bottom) shows that a similar even occurred in 1984, but was not associated with any eastward flow since the thermocline equatorward of 10°S remained very high in the aftermath of the El Niño event of 1982–83 (see discussion in section 5). Figure 18 shows that SECC volume transport peaked at about 3 to 9 Sv in the first half of each year preceding 1982, then fell to about 1 Sv in the second half of the year.

As in the case of the NECC, the SECC is also associated with an annual signal of low SSS during and after the time of strongest flow (Fig. 3). Eldin (1983) found that the SECC at 150°W was usually characterized by slightly lower salinity water than that of the surrounding SEC. Jarrige (1968) found that the SECC at 170°E was associated with a salinity minimum and that the higher the eastward transport, the lower the surface salinity. In early 1980 and 1981, the SSS at 10°S, 165°E (measured on the Noumea–Japan ship of opportunity route) was about 0.4 lower than on the CP track when SECC speeds were about 20 cm s^{-1}. Thus the advective SSS change, $u\partial S/\partial x$, was about −0.1 per month, which was sufficient to account for the annual surface freshening. However, in 1979, when the current was relatively weak, and in 1982 and 1984, when it was nearly absent, freshening occurred apparently without eastward advection.

5. El Niño of 1982–83

The first evidences of El Niño in the equatorial CP were the increasing rainfall and SST (Fig. 4), westerly winds and the dramatically lowered SSS (Fig. 3); these indicators would have been noticeable by August 1982. Data compiled by J. Sadler (personal communication, 1985) show that rainfall at Christmas Island (2°N, 157°W) rose rapidly in August 1982 and continued to climb to a peak of greater than 0.7 m month^{-1} during December 1982 and January 1983. Total rainfall from September 1982 to January 1983 was 2.81 m. Mean rainfall at Christmas Island was 0.76 m yr^{-1} for the period 1917 through 1972, with a previous maximum of 2.6 m yr^{-1} during the 1941 El Niño year (Taylor, 1973). Outgoing longwave radiation data taken during the 1982–83 El Niño (Rasmussen et al., 1983) suggest that the Christmas Island rainfall was a good index of precipitation over the central equatorial Pacific from about 140°W to the date line.

The El Niño is evident in the surface salinity record (Fig. 3) as an approximately −1 anomaly spanning the equator from about 5°N to 5°S starting in July–August 1982 and reaching a peak in October–November 1982. A quantity of 2.8 m of fresh water (equal to Christmas Island rainfall from September 1982 to January 1983) mixed into a 100 m layer of sea water of salinity 35.3 would produce a salinity decrease of 0.94; therefore,

the local rainfall was sufficient to account for a salinity signal of the magnitude observed. This also suggests that the low salinity extends throughout the upper layer, since, without mixing, the extreme local (and regional) precipitation would produce a much lower SSS. However, the low SSS peaked in October–November 1982, about two months before the local rainfall peaked, which implies that other mechanisms must have been important (Donguy and Eldin, 1985).

Figure 3 immediately suggests the possibility of advection of low SSS water from the north. Direct current measurements along 159°W (Firing et al., 1983; Firing, personal communication, 1985) show that the meridional component of near-equatorial surface currents was weak and generally northward during the period the SSS dropped, so southward advection appears unlikely. These current measurements also show that zonal currents spanning the equator during July and August 1982 were predominantly eastward in the upper 100 m at approximately 30 cm s^{-1} (the eastward flow increased with depth). Equatorial SSS measured on the Noumea–Japan track of the ship of opportunity network at 0°, 160°E was as low as 34.4 in July 1982, which is consonant with the heavy rainfall measured at Tarawa (1°N, 174°E) in that month (Donguy and Eldin, 1985) and also the negative OLR anomalies in that region. The advective term $u\partial S/\partial x$ (where u is taken to be the zonal velocity measured by Firing et al., 1983, and $\partial S/\partial x$ is estimated from the SSS difference between the CP and Noumea–Japan ship tracks) represents a salinity change of about −0.2 per month in the CP. The advective term is not quite enough to account for the drop in SSS, which was −0.4 per month during July, −0.5 per month in August, and −0.2 per month in September. A similar calculation using the SST from the two tracks leads to a similar conclusion.

Several features of the ocean–atmosphere anomalies that characterized the El Niño, including the heavy precipitation region, the westerly wind maximum, the SST maximum and the SSS minimum all appear to progress eastward into and across the central Pacific during July to October 1982, reaching their peaks in the CP between October and December 1982 (Donguy and Eldin, 1985). The collective data indicate that both advective and local effects contributed to the extreme low-salinity anomaly in the CP, but a clear separation of the relative contributions cannot be made.

In September 1982, the equatorial thermocline deepened by about 20 m and sharpened, with less than 35 m separating 27° and 18°C (Fig. 4). The pre-El Niño mean depth difference between 27° and 18°C was 85 m (Fig. 9). At this time the EUC nearly disappeared at 159°W, and in October and November an equatorial eastward jet developed at the surface with speeds up to 1.4 m s^{-1} (Firing et al., 1983), replacing the normal westward flow of the SEC at the equator. During the last months of 1982 the isotherm ridge at about 10°N shoaled more strongly than in any of the

other annual cycles of the six years studied; in the previous three years the minimum depths reached by the 20°C isotherm during the annual shoaling were 63, 62 and 59 m, whereas in November 1982, 20°C rose to 45 m (Fig. 11a, bottom). The combination of the very shallow isotherm ridge at 10°N and the deep, warm, fresh layer spanning the equator led to a strong meridional pressure gradient and increased eastward geostrophic transport in the NECC; the peak of 42 Sv occurred in November 1982 (Fig. 18). The 1982 peak in the thermoclinic estimate of NECC transport (Fig. 18) is smaller because some of the pressure gradient increase was due to warming and freshening in the surface layer at the southern edge of the NECC. Geostrophic speeds in the NECC near 5°N, which usually are maximal near 75 m, increased upward to a maximum of more than 90 cm s^{-1} at the surface in November 1982; this was associated with the very low density surface water. At this time eastward surface flow, consisting of the NECC and the eastward jet measured by Firing et al. (1983), extended from 10°N to 5°S, with a total eastward transport on the order of 60–70 Sv. The increase of dynamic height near the equator weakened the equatorward pressure gradient force driving the SEC near the equator, leaving only a remnant of this current south of 5°S (Fig. 14); SEC geostrophic transport over 2°–20°S fell by more than 10 Sv (Fig. 15). These events define the first stage of the El Niño in the CP, which lasted until early December 1982.

The second stage began in December 1982, when the equatorial upper thermocline shoaled approximately 50 m. The 20°C isotherm, which had been at 157 m at the equator in October 1982, rose to 110 m by February 1983 (Fig. 4). Isotherms above 20°C shoaled even more than this, while the 14°C isotherm was nearly unaffected. Firing et al. (1983) measured a return of both the EUC in the thermocline and the SEC at the surface in January. The equatorial thermocline continued shoaling until September 1983, with isotherms above 20°C at their highest level during the five years studied and the 26°C isotherm reaching the surface. Surface temperatures at the equator at the end of 1983 were more than 1°C colder than had been observed at any time during the previous eight years.

In the first half of 1983 the isotherm ridge at 10°N deepened to its lowest level of 1979–83; at 10°N the 20°C isotherm descended to 113 m in July 1983 (Figs. 11a, b). This occurred at the usual season of deepest ridge depths, but was about 20 m below the pre-El Niño July mean. The combination of the weak ridge at 10°N with the rise of the equatorial thermocline nearly eliminated the thermocline slope across the NECC (Fig. 19), and geostrophic volume transport in the NECC fell to less than 2 Sv by July. Westward surface geostrophic flow can be inferred from the equator to 8°N (Fig. 19), resulting in a broad SEC north of the equator (Fig. 14). Near 4°N the westward surface geostrophic speeds rose to 30 cm s^{-1} during this period;
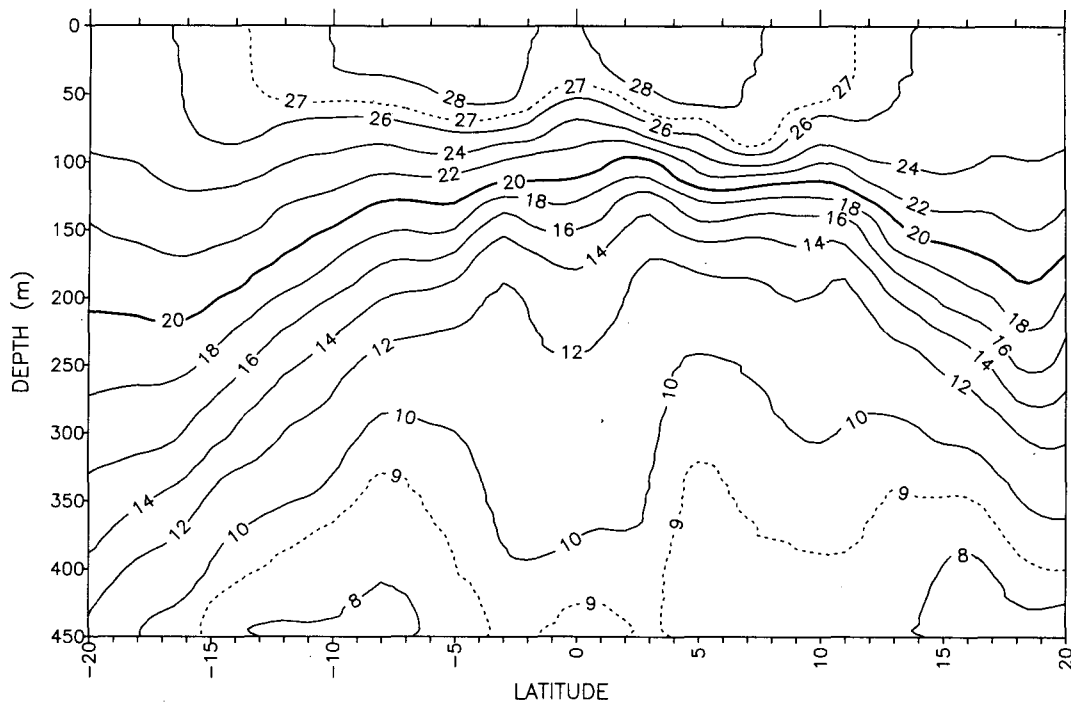
FIG. 19. Temperature (°C) on the CP track during July 1983.

the volume transport between 2° and 8°N was about 5 to 10 Sv during mid-1983.

South of the equator to about 12°S the thermocline shoaled at least 60 m during the first six months of 1983. Figure 11b shows that this anomaly occurred nearly simultaneously with the equatorial shoaling, resulting in an uplifted thermocline stretching across the equator from 5°N to 12°S (Fig. 19). Wyrtki (1984) noted that sea level at Funafuti Island (9°S, 179°E) dropped to 40 cm below normal by June 1983, which is consistent with the 35 dyn cm drop at 9°S on the CP track (Fig. 6). Wyrtki interpreted the changes in sea level as a southward displacement of the subtropical gyre. The downward thermocline slope, which ordinarily characterized the region from 5° to 15°S, was now found from 10° to 20°S and was associated with a fairly weak SEC (speeds about 15-20 cm s^{-1}); in this region there is usually near-zero or weak eastward flow. The westward flow occurred simultaneously with an anomalously high SSS south of 10°S (Fig. 3). Figure 19 shows that the strong thermocline uplift near 9°S resulted in eastward geostrophic flow (the SECC) from about 5° to 9°S; the geostrophic volume transport was about 10 Sv.

At the end of 1983, the thermal structure in the CP appeared to be returning to normal conditions (Fig. 11a), with the exception of equatorial upper-layer temperatures, which remained anomalously cool (Fig. 4). The pressure gradient across the NECC was reestablished and NECC transport rose to 20 Sv in December 1983; this transport was about 20% weaker than the

pre-El Niño O-N-D mean. From 4°N to 12°S the 20°C isotherm dropped from 60-80 m to only about 20 m above normal (Fig. 11a, top). At the beginning of 1984, however, thermocline shoaling anomalies similar to those of 1983 reappeared in the region from 5°N to about 10°S (Fig. 11). The depth of 20°C at the equator, which had fallen to 140 m (still 20 m above the pre-El Niño December mean) in December 1983, rose again to about 100 m. A similar magnitude of shoaling occurred in the Southern Hemisphere (Fig. 11). During June 1984 (Fig. 20) the thermocline uplift spanning the equator again nearly eliminated the pressure gradient associated with the NECC, and NECC transport fell to less than 5 Sv. At the end of 1984 a near-normal temperature profile was reestablished near the equator, but in early 1985 another similar but slightly weaker shoaling event occurred. When a 12-month running mean (Fig. 11a, middle panel), which contains much of the variance associated with the El Niño event, is removed from the depth of 20°C (Fig. 11a, bottom), these fluctuations appear to be in phase with the usual annual equatorial cycle of high (low) thermocline in the middle (end) of each year, although its amplitude was nearly twice as strong in 1983 and 1984 as for the pre-El Niño period.

6. Ekman pumping

In the extra-equatorial region, the simplest dynamical mechanism that can affect thermocline depth is Ekman pumping, in which the divergence of the Ek-
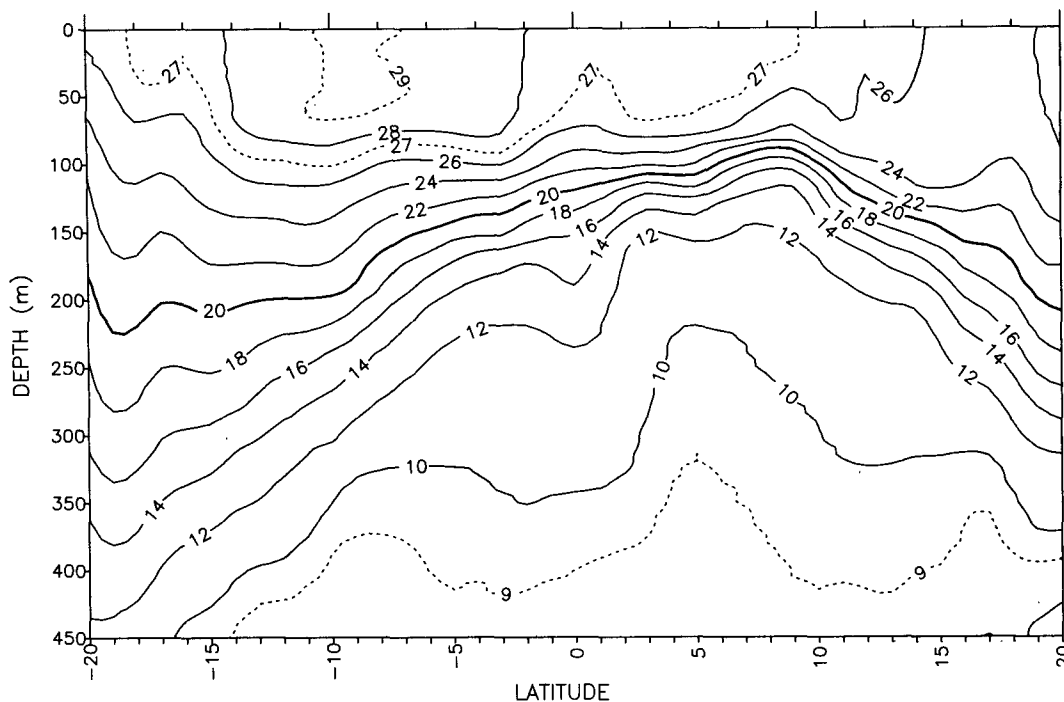
FIG. 20. As in Fig. 19 except for June 1984.

man transport balances the vertical motion at the bottom of the surface layer. In this section it is argued that observed large-scale vertical movement of the 20°C isotherm is in phase with the local Ekman pumping in much of the CP and that seasonal variations in the wind stress curl are in the correct sense to produce the observed variations in strength of the NECC and SECC. In addition, some of the anomalies associated with the El Niño of 1982–83 are found to be due to local Ekman pumping. The Ekman pumping dynamical balance is written

$$-\partial H/\partial t = \mathrm{curl}_z(\tau/\rho f),\qquad(2)$$

where H is the depth of the 20°C isotherm (positive down), τ the wind stress, ρ the density of seawater, and f the Coriolis parameter.

Meyers (1979) compared the vertical motion of the 14°C isotherm over much of the tropical Pacific with a model that allowed both Ekman pumping and the propagation of free nondispersive Rossby waves. Using annual harmonics of the wind stress field and the depth of 14°C, he found that near the isotherm ridge at about 12°N in the central Pacific the observed annual variations in isotherm depth were largely accounted for by Ekman pumping alone, although in the western Pacific the observed isotherm depth variations were larger than estimated by Ekman pumping. Near 6°N, Meyers (1979) found that Ekman pumping was not the dominant mechanism, but that annual isotherm depth variations propagated west at the phase speed for long Rossby waves.

In order to represent the annual variation in the wind field during 1979 through 1981, the three-year mean February and August wind stresses (Fig. 21) have been computed (see section 2 for description of this dataset). The average wind stress curl for the two months is shown in Fig. 22. The principal signals of interest are the annual changes in the intertropical convergence zone (ITCZ) at 5° to 12°N and the South Pacific convergence zone (SPCZ) at 5° to 15°S west of 150°W.

The cyclonic (upwelling) curl associated with the minimum of easterly stress in the ITCZ meanders annually; the maximum cyclonic curl is observed near 6°N in February and near 11°N in August (Fig. 22). The qualitative sense of Ekman pumping resulting from the variation in the position of the ITCZ is upward motion at the thermocline ridge near 10°N and downward motion at the thermocline trough near 4°N in the last half of each year (Fig. 22). This motion tends to increase the thermocline slope across the NECC. The opposite sense of Ekman pumping motion at 4° and 10°N occurs in the first half of each year, resulting in a decrease in thermocline slope.

In the southwest Pacific, the SPCZ appears in the southern summer as a region of cyclonic curl extending eastward from New Guinea to about 150°W (Fig. 22). During the southern winter, the SPCZ is replaced by southeast trade winds (Fig. 21). When the SPCZ is strong, in the early months of the year, the sign of pumping is upward at the south end of the CP track and downward between 10°S and the equator (Fig. 22), which tilts the thermocline down toward the equa-
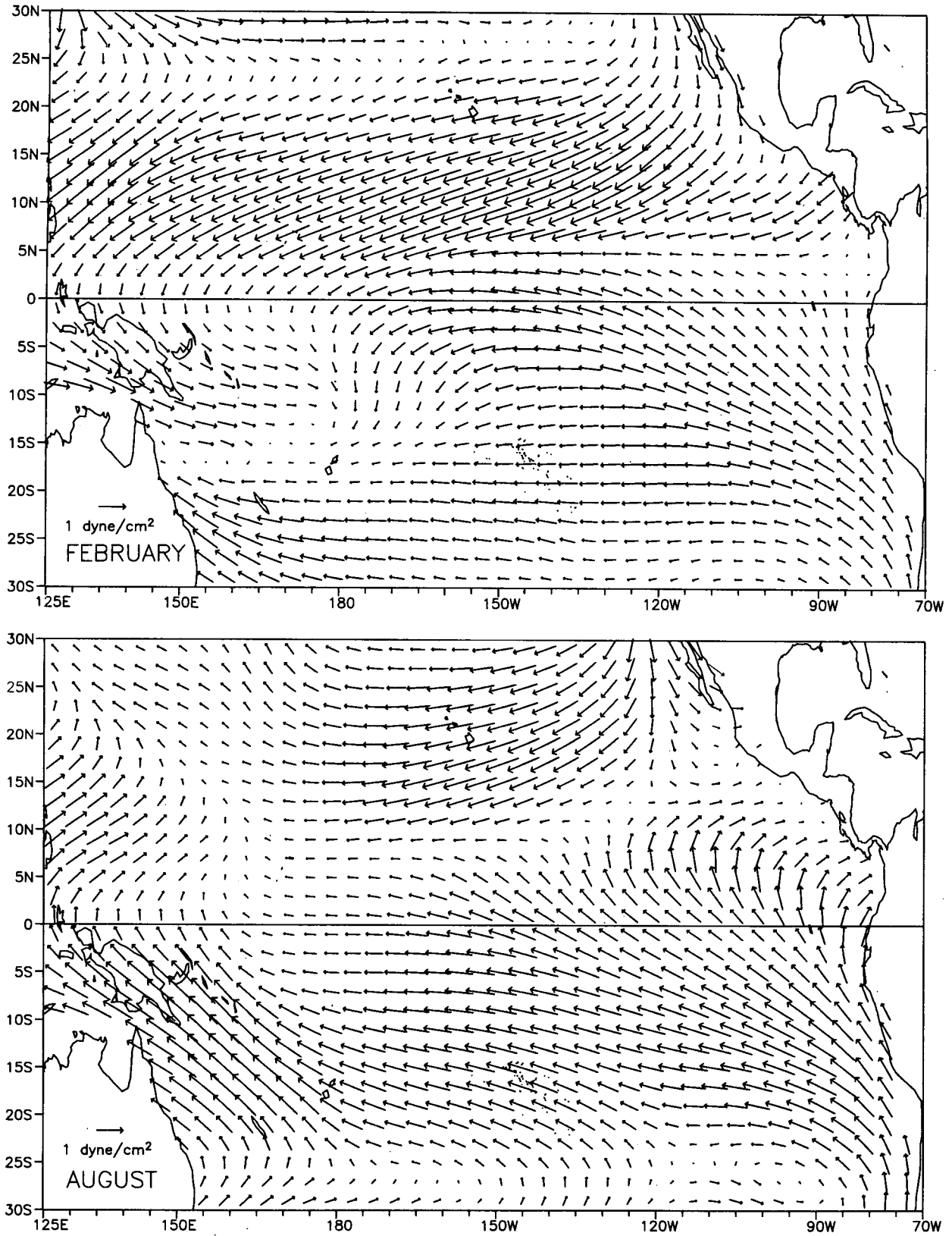
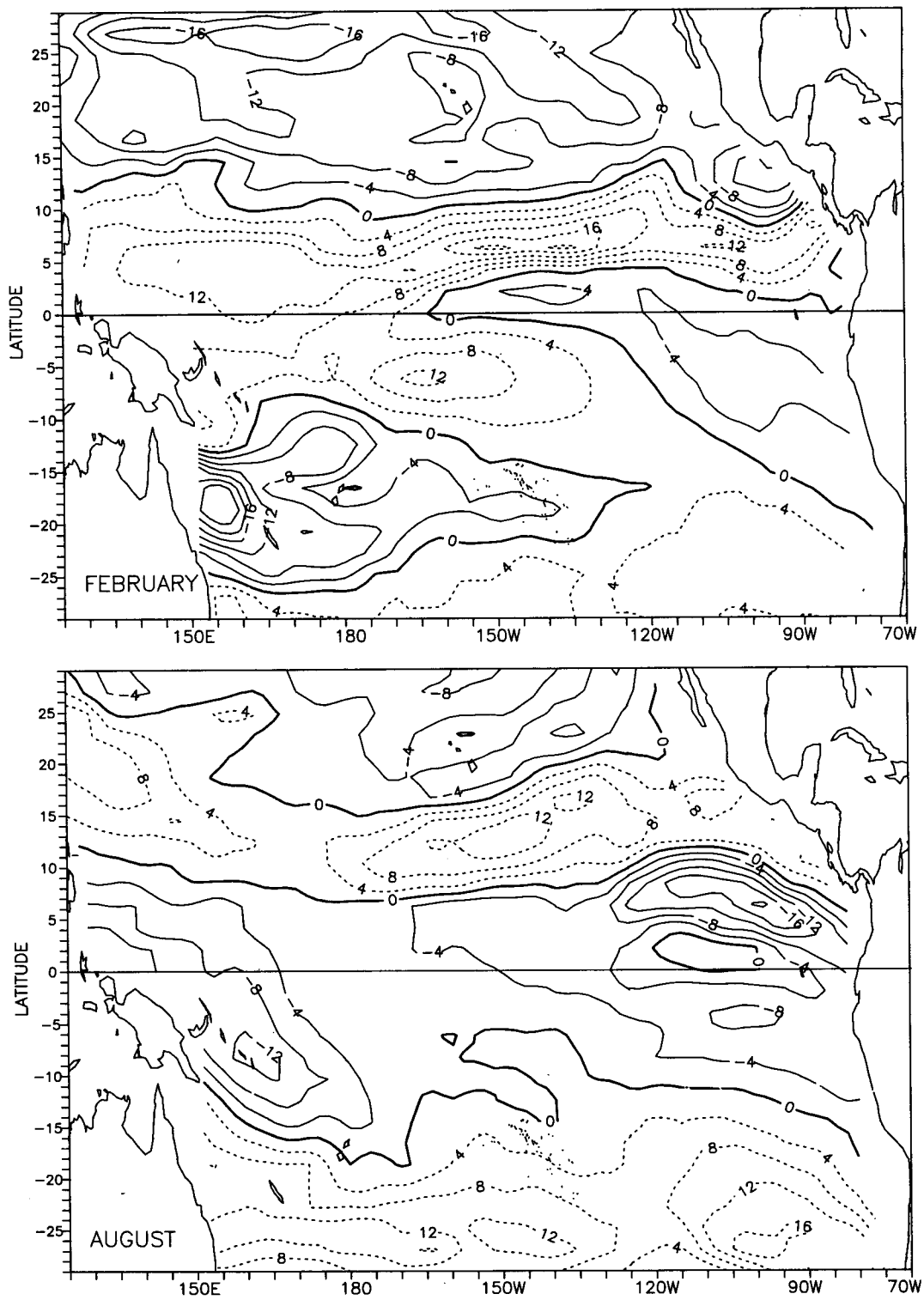FIG. 21. Mean wind stress during 1979–81. Top panel: February; bottom panel: August.

FIG. 22. Mean wind stress curl (10^{-8} N m^{-3}) during 1979–81. Cyclonic (Ekman upwelling) curl is positive (dashed contours) in the Northern Hemisphere and negative (solid contours) in the Southern Hemisphere. Top panel: February; bottom panel: August.

tor and implies eastward geostrophic flow (the SECC) near 10°S.

The Ekman pumping balance (2) has been computed for monthly values of the wind stress curl and the depth of the 20°C isotherm (Fig. 23) at selected latitudes on the CP track. Although the monthly time derivative of 20°C depth is a noisy variable (it has been smoothed by a ¼–½–¼ filter in Fig. 23), relatively high correlations are found between the terms of (2) in the CP, consistent with the preceding qualitative discussion. Correlations are highest near the isotherm ridge at 10°N and from 12° to 18°S, which are also regions where the phases of the first and second annual harmonics of these variables are closely matched (Fig. 24). The 36-month length of the time series studied is not sufficient to accurately estimate confidence limits for the correlation. The autodecorrelation time scales of $\partial H/\partial t$ and $curl_z(\tau/\rho f)$ on most of the CP track are 2 to 3 months, regardless of whether or not the annual cycle is removed. There are roughly 36/3 = 12 degrees of freedom, which indicates a 95% significance correlation level of 0.53. The correlation is at or above this level at 6° to 12°N and at 6°S and 12° to 18°S.

The amplitudes of the first harmonics of the terms of (2) are about 5 m month⁻¹, with a peak at the isotherm ridge at 10°N and a minimum near 8° to 10°S (Fig. 24). An estimate of the size of the error in the harmonics is obtained by computing the harmonic decomposition for each of the three years 1979–81 separately and finding the rms amplitudes and phases. The rms is a measure of how regular the harmonic cycles were during 1979–81. The rms amplitudes of the first harmonics are about 1.5 m month⁻¹, which implies
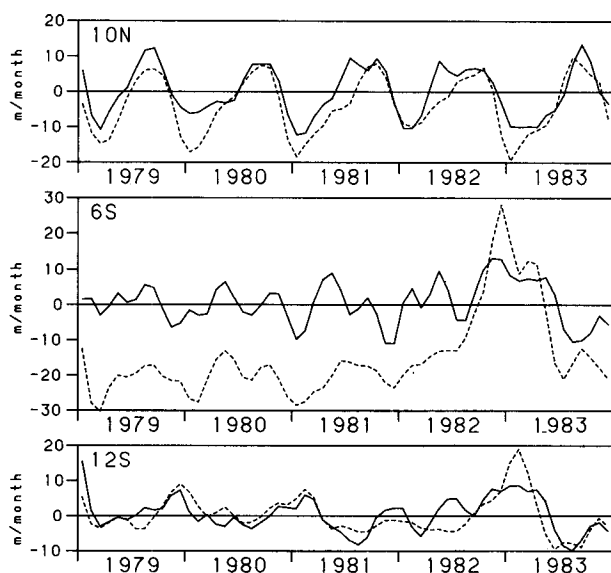

FIG. 23. Ekman pumping balance (m month⁻¹). Solid line is −∂H/∂t; dashed line is $curl_z(\tau/\rho f)$. Upward motion is plotted upward on the graph. Top panel: 10°N; middle panel: 6°S; bottom panel: 12°S.

that the amplitudes of $\partial H/\partial t$ and $curl_z(\tau/\rho f)$ shown in Fig. 24 probably do not differ significantly anywhere on the CP track. The rms phase of the first harmonics are about 1 month, with peaks of 2–3 months at 18°N and 8°–10°S where the amplitudes are weak (Fig. 24). The amplitudes of the second harmonics are about 3 m month⁻¹ in the CP (Fig. 24). The rms amplitudes are about 1 m month⁻¹; however, the phases varied more than the phases of the first harmonics during the 3 years studied, with rms of about 2 months. The phases of both the first and second harmonics of $\partial H/\partial t$ are nearly constant across the equatorial waveguide (Fig. 24), indicating that the equatorial thermocline fluctuates coherently at these frequencies.

At 10°N (Fig. 23) the correlation of the terms in (2) is 0.92. The amplitudes and phases of both the first and second harmonics are in close agreement in this region (Fig. 24) and account for the high correlations. This confirms and strengthens Meyers' (1979) finding that Ekman pumping is the dominant mechanism in annual variations of the depth of the thermocline at the CCT and, hence, a major controlling factor in NECC transport variation.

Within 5° of the equator the correlations are low. The right-hand side of (2) can be decomposed into two terms:

$$curl_z\left(\frac{\tau}{\rho f}\right) = \left(\frac{1}{f}\right)curl_z\left(\frac{\tau}{\rho}\right) + \left(\frac{\beta}{f^2}\right)\left(\frac{\tau^x}{\rho}\right),$$

where β is the meridional derivative of the Coriolis parameter. The second term is proportional to $1/f^2$ and increases in relative importance near the equator. The value of τ^x is nearly always negative in the CP, so this term adds a mean negative value to $curl_z(\tau/\rho f)$, and the Ekman pumping balance does not hold for latitudes less than about 6°. For example, at 6°S before the El Niño, Ekman pumping was strongly downward (the 1979–81 mean was −21 m month⁻¹) (Fig. 23), although $curl_z\tau$ takes both positive and negative values during the average year (Fig. 22). At 4°N, mean pumping was 40 m month⁻¹ downward. Although correlation of the first (curl) term with $\partial H/\partial t$ is 0.77, in accordance with the qualitative annual cycle shown in Fig. 22, τ^x is negatively correlated with $\partial H/\partial t$ and the correlation of the entire term is 0.44. Ekman pumping is probably not the primary dynamics that affects thermocline depth at 4°N; because 4°N is within the equatorial waveguide, $\partial H/\partial t$ is, in part, determined by propagation of remotely forced waves. However, the phases of both the first and second annual harmonics of $\partial H/\partial t$ and $curl_z(\tau/\rho f)$ differ by only about one month at 4°N (Fig. 24), so local forcing still may play a significant role.

At 6°S, on the northern side of the SECC, the correlation between the terms of (2) is 0.51. The phase of the annual cycle of the curl lagged the phase of $\partial H/\partial t$ by about 50 days (Fig. 24); this may not be a significant difference since the rms uncertainty of each phase es-

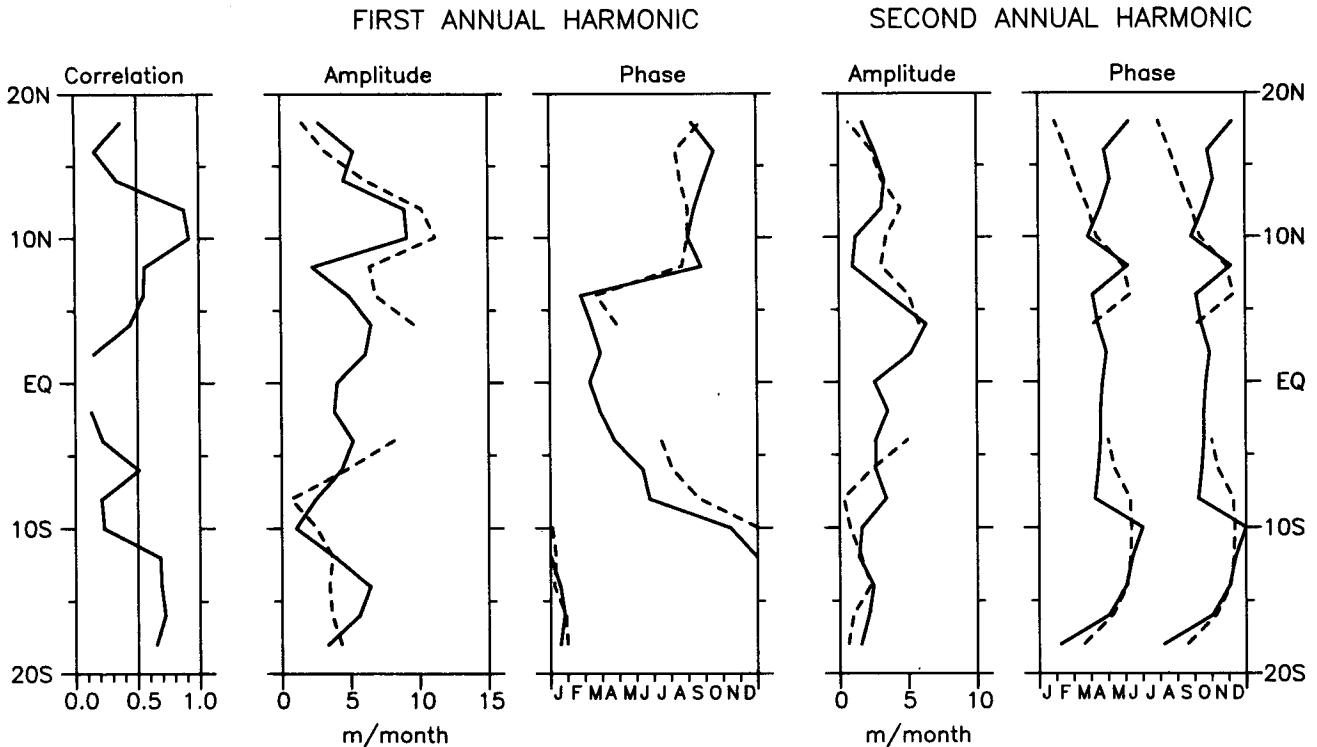FIRST ANNUAL HARMONIC   SECOND ANNUAL HARMONIC

FIG. 24. (Left panel) Correlation of the terms of Eq. (2) for the period 1979–81. (Middle panels) Amplitude and phase of the first annual harmonic of $\partial H/\partial t$ and $\text{curl}_z(\tau/\rho f)$. (Right panels) Amplitude and phase of the second harmonic of $\partial H/\partial t$ and $\text{curl}_z(\tau/\rho f)$. Phase plot shows both peaks, ½ year apart. Solid line is $\partial H/\partial t$; dashed line is $\text{curl}_z(\tau/\rho f)$ in each case. Phase is shown as the time of maximum upward vertical motion.

timate is one month. At 12°S (Fig. 23, bottom), on the southern side of the SECC, the correlation was 0.68 and the fluctuations of both $\text{curl}_z(\tau/\rho f)$ and $\partial H/\partial t$ had closely matched phases of both first and second harmonics (Fig. 24). As in the case of the NECC, the poleward side of the SECC has a large fraction of variance at the annual frequency and appears to be dominated by Ekman pumping, while the equatorward side of both countercurrents may be more subject to other influences.

The most prominent thermocline depth anomaly associated with the El Niño of 1982–83 was the uplift over 5°N to 15°S that occurred in early 1983 (Fig. 11b). Figure 25 shows that in the first months of 1983 winds on the CP track were westerly from just south of the equator to about 10°S. This produced strong cyclonic curl in the region from about 5° to 20°S, which was closely correlated with the rise of 20°C observed at this time, and Eq. (2) nearly balances (Fig. 23, middle panel). It can be concluded from Figs. 11 and 25 that this pattern was typical for latitudes from 4° to 16°S. Thus, the large Southern Hemisphere extra-equatorial El Niño anomaly of 1983 can be attributed to anomalous local wind forcing through the mechanism of Ekman pumping. The raised thermocline at 8° to 10°S was associated with a relatively strong SECC in the first six months of 1983 between 10° and 5°S (Fig. 14).

The annual cycle of the SECC implied by the annual variation of wind stress curl (Fig. 22) leads to the conclusion that the SECC is confined to the western part of the South Pacific, since the upward Ekman pumping is due to the SPCZ, which is only found over the western part of the basin. This idea is supported by calculation of the Sverdrup transport from the mean (1979–81) wind stress. The Sverdrup transport is given by

$$\beta V = \text{curl}_z(\tau/\rho), \qquad (3)$$

where V is the total (Ekman plus geostrophic) meridional volume transport (Sverdrup, 1947). The zonal volume transport is found by assuming horizontal nondivergence of total transport and integrating from the eastern boundary, where the zonal transport is assumed to be zero. Streamlines of volume transport are shown in Fig. 26; the SECC is seen as a weak eastward flow near 10°S west of the dateline. This eastward transport is due to the wind pattern associated with the SPCZ; farther east the Sverdrup transport is uniformly westward.

7. Summary

XBT and surface salinity data from the ship of opportunity program have been used to estimate dynamic height and geostrophic flow in the central Pacific. In
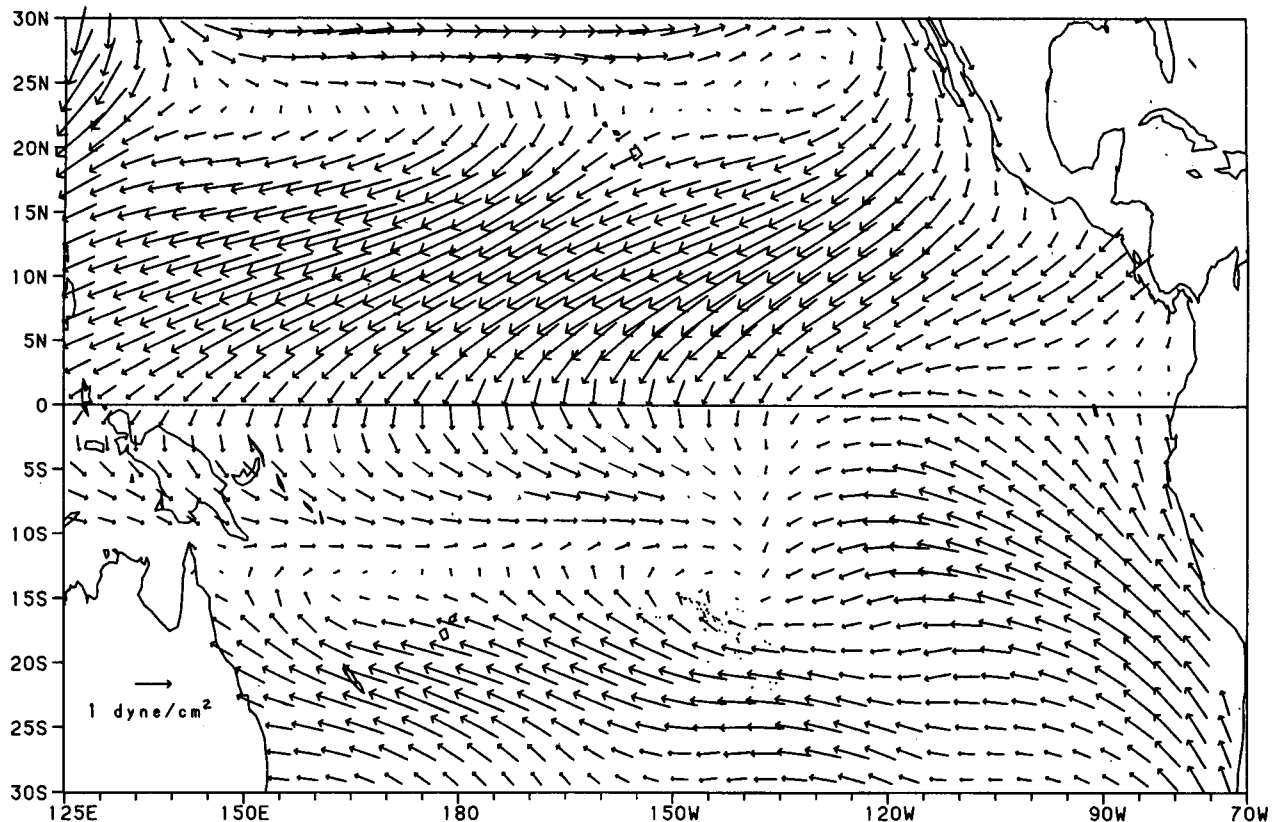
FIG. 25. Mean wind stress for the period December 1982 through February 1983.

the thermocline and below, salinity is estimated from a mean T-S relation. The surface salinity is known; above the thermocline the salinity profile is assumed to have the same functional form as the temperature profile. Dynamic heights calculated by this method are significantly more accurate than those found using a mean T-S relation in the upper water column. Salinity variations were particularly important during the 1982–83 El Niño, when very low salinity water in the upper layer raised dynamic heights by about 6 dyn cm near the equator and accounted for an important fraction of the anomalous pressure gradients observed.

Thermocline fluctuations have a large annual component in the central Pacific; out-of-phase annual fluctuations at the isotherm ridge near 10°N and the trough near 4°N are associated with variability in the NECC, and a similar oscillation between 6° and 15°S is associated with the SECC. The SECC is observed to be present only in the first few months of the year. NECC variability can be accurately represented by a model assuming a two-layer ocean, except during the El Niño of 1982–83, when warming and freshening in the surface layer was a significant factor. The isotherm ridge near 10°N, which forms the boundary between the NEC and NECC, meanders poleward at the end of the year when the pressure gradient across the two currents is strongest and meanders equatorward at the middle

of the year when the pressure gradients are weakest. The meander tends to cancel the effect of the annual variation of pressure gradient; the annual fluctuation of NECC transport is much less strong than would be expected solely from the pressure gradient fluctuation. Since the strongest flow in the NEC is found near its southern boundary, it is essential to measure the current all the way to the CCT to accurately estimate transport. The use of island sea-level differences as an index of NEC transport introduces significant errors because the islands do not span the full extent of the meandering current. There is a significant annual variation in the baroclinic structure of the NEC. The current extends deeper during the period of weakest pressure gradient, which tends to weaken the transport fluctuation. When all processes that affect NEC transport are taken into account, little annual transport variability is observed.

There were two distinct stages of the El Niño of 1982–83 in the CP. In late 1982, equatorial dynamic heights rose about 15 dyn cm, increasing the pressure gradient across the NECC and increasing NECC transport to more than 40 Sv. In the second stage, at the beginning of 1983, the thermocline shoaled 50–60 m from 5°N to 12°S. This was associated with a very weak NECC. The thermocline remained anomalously high through the end of 1984.
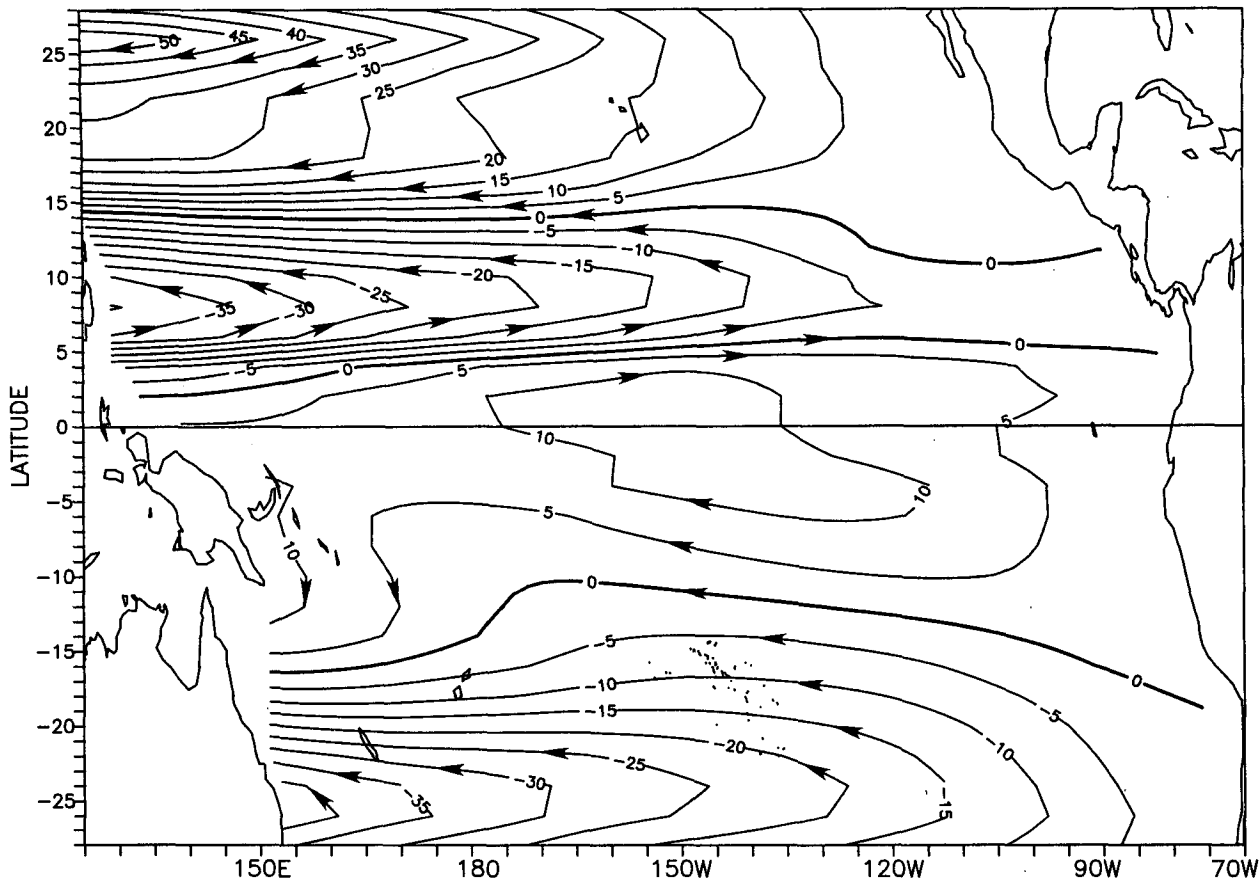
FIG. 26. Streamlines of volume transport (each contour represents 5 Sv) computed from the Sverdrup relation using the average wind stress from 1979 through 1981.

The annual cycle of wind stress curl (Ekman pumping) is qualitatively consistent with observed thermocline depth fluctuations in much of the CP, including the annual cycles of the NECC and SECC. At 10°N and near 15°S, it is the dominant mechanism. At the beginning of 1983, anomalous westerlies near 5°–10°S were associated with strong cyclonic (Ekman upwelling) curl, which closely correlated with the observed thermocline shoaling. Thus the strongest extra-equatorial anomaly of this El Niño in the CP can be interpreted as a response to local wind forcing.

REFERENCES

Cantos-Figuerola, A., and B. A. Taft, 1983: The South Equatorial Current during the 1979–80 Hawaii–Tahiti Shuttle. *Trop. Ocean-Atmos. Newslett.,* **19,** 6–8.

Donguy, J.-R., and G. Eldin, 1985: Eastward propagation at the equator during the 1982–83 El Niño inferred from sea surface salinity. *Trop. Ocean-Atmos. Newslett.,* **32,** 1–2.

Eldin, G., 1983: Eastward flows of the south equatorial central Pacific. *J. Phys. Oceanogr.,* **13,** 1461–1467.

Emery, W. J., and R. T. Wert, 1976: Mean *T–S* curves in the Pacific and their application to dynamic height computations. Scripps Institution of Oceanography, Rep. SIO 76-6.

——, and J. S. Dewar, 1982: Mean temperature–salinity, salinity–depth and temperature–depth curves for the North Atlantic and the North Pacific. *Prog. Oceanogr.,* **11,** 219–305.

Firing, E., C. Fenander and J. Miller, 1981: Profiling current meter measurements from the Norpax Hawaii to Tahiti Shuttle Experiment. University of Hawaii, Ref. HIG-81-2.

——, R. Lukas, J. Sadler and K. Wyrtki, 1983: Equatorial Under-

current disappears during 1982–83 El Niño. *Science,* **222,** 1121–1123.

Goldenberg, S. B., and J. J. O'Brien, 1981: Time and space variability of tropical Pacific wind stress. *Mon. Wea. Rev.,* **109,** 1190–1207.

Hayes, S. P., 1982: A comparison of geostrophic and measured velocities in the Equatorial Undercurrent. *J. Mar. Res.,* **40,** 219–229.

Jarrige, F., 1968: On the eastward flow of water in the western Pacific south of the equator. *J. Mar. Res.,* **26,** 286–289.

Kendall, T. R., 1970: The Pacific Equatorial Countercurrent. Ph.D. thesis, Nova University.

Kessler, W. S., B. A. Taft and M. McPhaden, 1985: An assessment of the XBT sampling network in the central Pacific. Univ. Corp. for Atmos. Res., USTOGA 4, 62 pp.

Liebmann, B., and D. L. Hartmann, 1982: Interannual variations of outgoing IR associated with tropical circulation changes during 1974–78. *J. Atmos. Sci.,* **39,** 1153–1162.

Lukas, R., and E. Firing, 1984: The geostrophic balance of the Pacific Equatorial Undercurrent. *Deep-Sea Res.,* **31,** 61–66.

McPhaden, M., 1984: On the dynamics of equatorial subsurface countercurrents. *J. Phys. Oceangr.,* **14,** 1216–1225.

Merle, J., H. Rotschi and B. Voituriez, 1969: Zonal circulation in the tropical western South Pacific at 170°E. *Bull. Japan. Soc. Fish. Oceanogr.,* Special Number (Prof. Uda's Commemorative Papers), 91–98.

Meyers, G., 1975: Seasonal variation in transport of the Pacific North Equatorial Current relative to the wind field. *J. Phys. Oceanogr.,* **5,** 442–449.

——, 1979: On the annual Rossby wave in the tropical North Pacific Ocean. *J. Phys. Oceanogr.,* **9,** 663–674.

——, and J.-R. Donguy, 1980: An XBT network with merchant ships. *Trop. Ocean-Atmos. Newslett.,* **2,** 6–7.

Patzert, W. C., 1969: Eddies in Hawaiian waters. University of Hawaii, Ref. HIG-69-8.

Rasmussen, E. M., P. A. Arkin, A. F. Krueger, R. S. Quiroz and R. W. Reynolds, 1983: The equatorial Pacific atmospheric climate during 1982–83. *Trop. Ocean-Atmos. Newlett.,* **21,** 2–3.

Reid, J. L., 1959: Evidence of a South Equatorial Countercurrent in the Pacific. *Nature,* **184,** 209–211.

——, 1961: On the geostrophic flow at the surface of the Pacific Ocean with respect to the 1000-decibar surface. *Tellus,* **13,** 489–502.

Rotschi, H., P. Hisard and F. Jarrige, 1972: Les Eaux du Pacifique Occidental a 170°E entre 20°S et 4°N. Travaux et Documents de l'ORSTOM, **19.**

Sadler, J. C., and B. J. Kilonsky, 1983: Meteorological events in the central Pacific during 1983 associated with the 1982–83 El Niño. *Trop. Ocean-Atmos. Newslett.,* **21,** 3–5.

——, and ——, 1985: Deriving surface winds from satellite observations of low-level cloud motions. *J. Climate Appl. Meteor.,* **24,** 758–769.

Seckel, G. R., 1975: Seasonal variability and parameterization of the Pacific North Equatorial Current. *Deep-Sea Res.,* **22,** 379–401.

Sverdrup, H. U., 1947: Wind-driven currents in a baroclinic ocean, with application to the equatorial currents of the eastern Pacific. *Proc. Nat. Acad. Sci.,* **33,** 318–326.

Taylor, R. C., 1973: An atlas of Pacific island rainfall. University of Hawaii, Ref. HIG-73-9.

Wyrtki, K., 1974a: Sea level and the seasonal fluctuations of the equatorial currents in the western Pacific Ocean. *J. Phys. Oceanogr.,* **4,** 90–103.

——, 1974b: Equatorial currents in the Pacific 1950 to 1970 and their relations to the trade winds. *J. Phys. Oceanogr.,* **4,** 372–380.

——, 1974c: The dynamic topography of the Pacific Ocean and its fluctuations. University of Hawaii, Ref. HIG-74-5.

——, 1982: Eddies in the Pacific North Equatorial Current. *J. Phys. Oceanogr.,* **12,** 746–749.

——, 1984: A southward displacement of the subtropical gyre in the South Pacific during the 1982–83 El Niño. *Trop. Ocean-Atmos. Newslett.,* **23,** 14–15.

——, and T. R. Kendall, 1967: Transports of the Pacific Equatorial Countercurrent. *J. Geophys. Res.,* **72,** 2073–2076.

——, and B. J. Kilonsky, 1984: Mean water and current structure during the Hawaii-to-Tahiti Shuttle Experiment. *J. Phys. Oceanogr.,* **14,** 242–254.

——, E. Firing, D. Halpern, R. Knox, G. J. McNally, W. C. Patzert, E. D. Stroup, B. A. Taft and R. Williams, 1981: The Hawaii to Tahiti Shuttle experiment. *Science,* **211,** 22–28.